Small-scale bedforms and associated sediment transport in a macro-tidal lower shoreface

Q. Guerrero[a], M. E. Williams[b,c], J. Guillén[a], I. D. Lichtman[b], P. D. Thorne[b], L. O. Amoudry[b]

[a]Institut de Ciències del Mar (ICM-CSIC), Passeig Marítim de la Barceloneta 37-49, 08003 Barcelona Spain.

[b]National Oceanography Centre, Joseph Proudman Building, 6 Brownlow Street, Liverpool L3 5DA, UK.

[c]Departamento de Obras Civiles, Universidad Técnica Federico Santa María, Avenida España 1680, Valparaíso, Chile.

Corresponding author: Jorge Guillén; e-mail: jorge@icm.csic.es

Abstract

Ripples and small-scale bedforms are ubiquitous in shallow water environments under the combined action of currents and waves. Small scale processes linked to their formation and migration are interconnected with sediment transport at larger scales (e.g. tens of metres to kilometres), both resulting in and being affected by large scale sediment transport and geomorphological evolution. The lower shoreface provides a key link between coasts and continental shelves, but the contribution of ripples and small-scale bedforms to sediment transport in this region has yet to be fully addressed. This work presents a study of sediment dynamic processes on the lower shoreface in the presence of small-scale bedforms. Observations were made during the winter of 2017 on the lower shoreface of Perranporth Beach, which is in the south west of the UK and exposed to Atlantic waves. The analysis of morphological expressions and the variability of ripples under waves, currents and wave-current conditions are assessed. Ripple morphology and associated dynamics are analysed for their potential contribution to the exchange of sediment between the lower and the upper shoreface. In the present study it was observed that even though ripples were evolving depending on the wave-current forcing, little ripple migration was observed due to low wave skewness. The implication is that ripple migration and bedload transport are only a small contribution to onshore sediment transport under low to moderate energy conditions. However, during more energetic conditions, ripples were washed out and the wave skewness increased, resulting in onshore sediment transport under a sheet flow regime. This suggests that ripple formation and migration can have little impact on the cross-shore supply of sediment from the lower shoreface to the upper shoreface and that more energetic wave conditions are required to significantly transport sediment towards the beach.

Keywords: time-series, vortex ripples, sediment exchanges, ripple thresholds, lower shoreface

Highlights:

- High-resolution observations on the seabed reveal 2D and 3D wave vortex ripples in a macrotidal sandy lower shoreface, oriented almost parallel to the coastline.
- The morphological ripple transitions provide assessment of sediment transport regime thresholds.
- The hypothesis of cross-shore sediment supplied from the lower to the upper shoreface through ripple migration is not supported in the present study.

1. Introduction

Ripples are the most common and smallest bedform type on sandy seabeds, under low to intermediate flow conditions, between the thresholds for grain movement and sheet flow (Dalrymple and Rhodes, 1995). They are essential to bottom boundary layer processes through the interacting triad of hydrodynamics, mobile seabed, and transport of sediment particles (Nielsen, 1981; Davies and Thorne, 2008). Bedload sediment transport is partially attributed to ripples transport by the growth, morphological change, dynamism and migration, while the uneven bed alters boundary layer dynamics and the resulting suspended sediment dynamics and fluxes. Ripples also act as a key control on the bed shear stress by influencing the partition between skin friction and form drag, effective bed roughness, and near-bed velocity structure (Glenn and Grant, 1987; Grant and Madsen, 1979; Wiberg and Nelson, 1992; Li et al., 1996; Li and Amos, 1998, Hurther and Thorne, 2011).

Several ripple classification schemes exist. Ripples are morphologically classified based on their crest planform into straight-crested (two-dimensional) ripples, or sinuous and linguoid (three-dimensional) ripples (Allen 1968, Baas et al., 2016). Clifton and Dinger (1984) classified ripples as orbital, anorbital or suborbital when ripple wavelength respectively scales with the wave orbital diameter, the sediment grain size or both. Ripples are also classified based on the processes controlling sediment grain motion into rolling-grain, vortex, and post-vortex ripples. Rolling-grain ripples form on flat beds under oscillatory flows just above the threshold for grain motion. They typically remain small with low ripple steepness (η/λ with η the ripple height and λ the ripple length) values less than 0.1 (Bagnold, 1946; Rousseaux, 2006) and are the precursor of vortex ripples. As flow forcing (i.e. velocities) increases, ripples become steeper, and with steepness values in the range of 0.1-0.2 a lee side eddy may form, trapping sediment eroded from the ripple surface, and forming vortex ripples (Bagnold, 1946; Traykovski et al., 1999; Thorne al., 2009, Hurther and Thorne 2011; Nelson et al., 2013). Vortex ripples are generally triangular, symmetric and ripple steepness ratio is ~0.1-0.25. Their formation is related to waves when the ratio between the orbital diameter (d_0) and the median sediment grain size (d_{50}) is less than 5000 and they reach equilibrium rapidly. The presence of lee side eddies ejects sediment higher into the water column at flow reversal (Bagnold, 1946; Clifton and Dingler, 1984, Thorne et al., 2003, Davies and Thorne, 2005), thus contributing to increased sediment resuspension. As velocities increase further, orbital diameters become larger and when $d_0/d_{50} > 5000$, ripple height decreases but ripple wavelength remains unchanged, resulting in decreasing steepness (<0.15) and so-called post-vortex ripples, and eventually further progression to sheet flow (Clifton and Dingler, 1984). Similarly, under wave conditions, Thorne et al. (2009) distinguished between 2D steep ripples $\left(\frac{\eta}{\lambda} \geq 0.12\right)$, 2-3D transitional ripples $\left(0.08 \leq \frac{\eta}{\lambda} \leq 0.12\right)$ and dynamically plane bed $\left(\frac{\eta}{\lambda} \leq 0.08\right)$, observing different boundary layer flow characteristics for each one and roughly similar to the vortex, post-vortex and wash-out ripples respectively.

The transitional region between the breaker zone and the continental shelf, where changes on the beach profile are no longer discernible but seabed agitation by waves is still significant, is commonly referred to as the lower shoreface. The boundary between upper and lower shoreface is a very variable range and is approximately located at 6-10 m water depth. We refer the interested reader to the recent reviews of Anthony and Aagaard (2020) and Hamon-Kerivel et al. (2020) for detailed discussions of this zone. The lower shoreface is an essential element of coastal geomorphology as it potentially is a vast source of sediment for coastal landforms and accurate coastal sediment budgets would then need to consider exchanges with the lower shoreface (e.g. Valiente et al., 2019b). However, high-resolution observational studies of sediment transport, and in particular of bedload transport, are still rare (Anthony and Aagaard, 2020) due to a range of technical and logistical difficulties. Ripple migration, wash-out or sheet flow can be mechanisms of net bedload transport (Traykovski et al., 1999; Camenen and Larson, 2006; van Rijn, 2007a). One implication is that bedload transport may be inferred from observations of ripples and their migrations.

Cross-shore sediment exchange between the upper and the lower shoreface is mainly wave-driven, related to wave asymmetry and wave induced currents (as undertow), although coastal ocean currents (due to tides, winds, and other processes) can also transport sediment (Wright et al., 1991; Styles and Glenn, 2005; Ruessink et al., 2011). In the absence of currents, wave asymmetry is the primary mechanism for ripple migration. Asymmetries are required as linear, monochromatic waves will have equal velocities on each half wave cycle and thus no net sediment is transported (i.e. bedform migration) (Traykovski et al., 1999).

The general and theoretical understanding of bedform contribution to sediment transport is that the bedform migration component is onshore and large compared with the suspended component in relatively deep water and becomes progressively smaller with respect to the suspended transport towards the shore, through the shoaling and surf zone (Miles and Thorpe, 2015). However, Crawford and Hay (2001) observed offshore ripple migration during storm growth and onshore migration during storm decay, with the bedform migration highly correlated with the near-bed wave orbital velocity skewness in both cross-shore directions. Therefore, the relative contribution of bedform migration to sediment exchanges in the lower shoreface remains an open question.

The current study presents high-resolution observations of near-bed hydrodynamics and ripples on a macrotidal lower shoreface during winter (January-February) 2017 and evaluates the potential contribution of these bedforms to sediment exchanges between the lower and upper shoreface. The study was conducted in an embayed beach system at an intermediate point between the depth of closure based on the morphological change and the depth of transport considered as the boundary of intense sediment transport (upper-plane bed transition) (Valiente et al., 2019a). These observations provide new direct observations of small-scale dynamics and resulting sediment fluxes and transport on the lower shoreface of such an embayed system. These can provide new insights into the potential return of sediment from the lower shoreface to the beach and the potential role of small-scale bedforms in onshore sediment transport outside the breaking zone during calm and mild energy conditions. We introduce and describe the study site in section 2 and the observational methods in section 3. Results are presented in section 4 and discussed in section 5.

2. Study area

The study area is located offshore of Perranporth Beach (PB), in the southwest of England (Fig. 1a). The coastline of the southwest of England typically consists of hard rock cliffs interspaced by embayed sandy beaches. It is exposed to macro- to hyper-tidal ranges (mean spring tide range (MSR) from 4 to 12 m) and medium- to high-energy waves from the Atlantic Ocean (Scott et al., 2016). Located on the northwest coast of Cornwall, Perranporth Beach is a predominantly sandy beach with a semi-diurnal macro-tidal regime (mean neap and spring tidal ranges of 3.1 m and 6.1 m) (Austin et al., 2010; Inch et al., 2017). The beach is 3.5 km long and has an intertidal area ~200-300 m wide, which widens at the southern end to ~400 m (Fig. 1 b). PB is backed by an eroding sand dune system with steep vegetated dunes reaching nearly a mile inland, and by Devonian hard rock cliffs at the north and south ends of the beach (Fig. 1 b) (Poate et al., 2014; Scott et al., 2016).

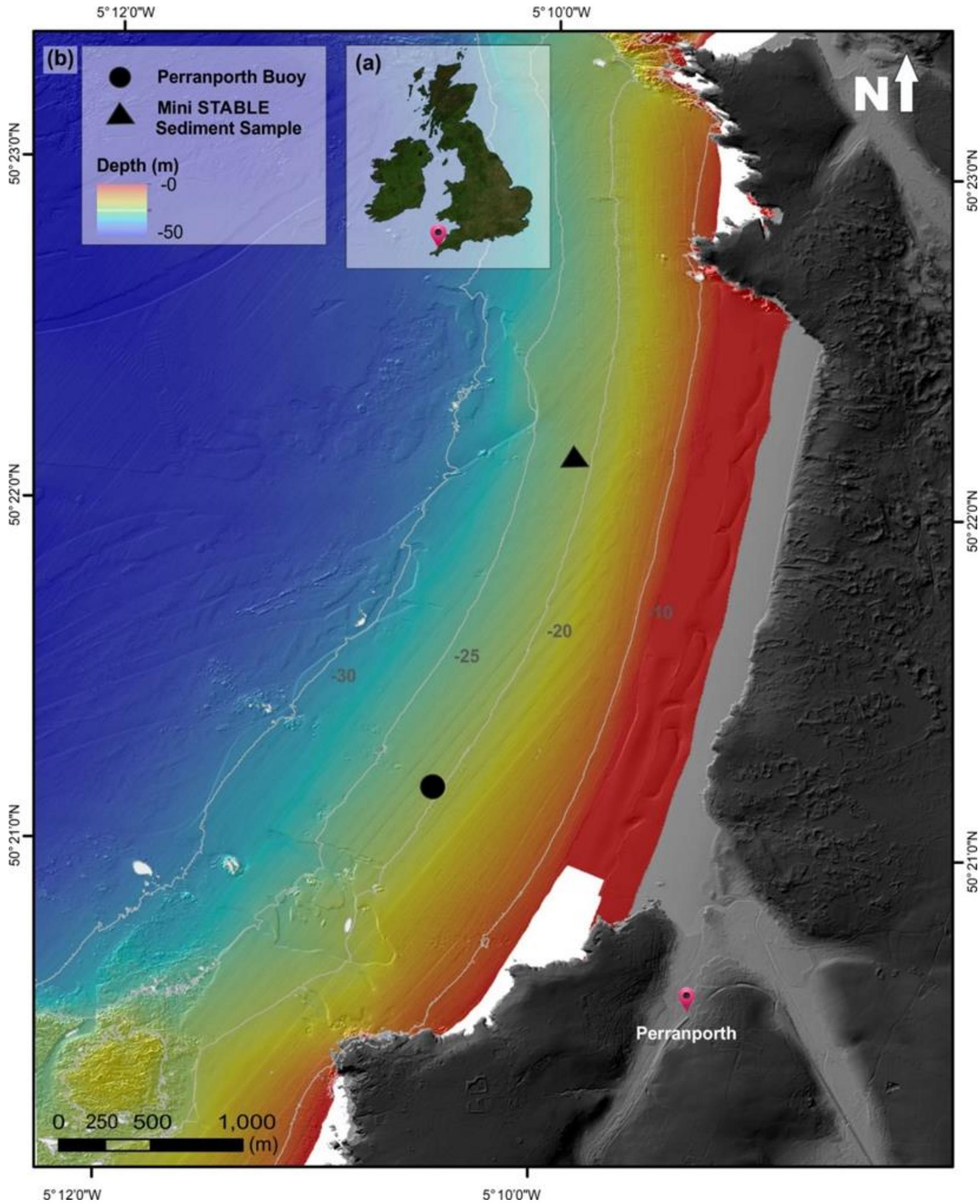

Figure 1.- Study area. (a) Location of Perranporth study area and (b) shaded-relief of Composite Digital Terrain Model (DTM) at 1 m resolution from LIDAR data available at http://environment.data.gov.uk and

bathymetry at 2 m resolution from UKHO INSPIRE Portal & Bathymetry DAC referenced to the Ordnance Datum Newlyn (ODN). The bathymetric contours are displayed every 5 m. The Mini-STABLE rig location is indicated with a black triangle and the offshore Buoy of Perranporth location is indicated with a black circle. The detailed geo-referenced shaded-relief images had sun-illumination with an azimuth of 315° and an elevation of 20° and two times vertical exaggeration of bathymetry dataset to highlight the morphological details of the seabed.

PB is relatively straight, facing the west-northwest towards the Atlantic (shoreline 11° from North) so it is fully exposed to the dominant westerly waves approach, receiving both Atlantic swell and locally generated wind waves (Austin et al., 2010; Inch et al., 2017). The mean annual significant wave height (H_s) and mean peak period (T_p), measured by the coastal Perranporth wave buoy during the period 2006- 2019, were 1.58 m and of 10.6 s, respectively, and significant wave height with an annual return period is 6.28 m (Channel Coastal Obervatory, 2020). High atmospheric pressure and northerly wind are also observed to cause northerly waves, which are small but energetically significant (Poate et al., 2014). The wave climate has a marked seasonality, with wave height and wave periods increasing during winter months. The monthly averaged H_s and T_p values from the coastal Perranporth wave buoy (from the same 2006 to 2019 record) range from 1.12 m and 9.0 s in June to 2.24 m and 12.4 s in January (Channel Coastal Obervatory, 2020). For the period of this study, January to March 2017, the monthly averaged H_s values were 1.57, 2.10 and 2.04 m and the corresponding $T_p$values 11.0, 12.7 and 12.2 s (Channel Coastal Obervatory, 2020). The shoreline location also displays high variability as a consequence of this weather seasonality (Davidson et al., 2017). From November to February shoreline retreat occurs in response to a succession of erosive storms, while beach recovery begins in late March, at slower rate (~1/4) than the retreat, often persisting until October (Davidson et al., 2017).

Following Wright and Short (1984), PB is a low-tide bar and rip with typically single or double subtidal bars located around the seaward limit of the surf zone (Scott et al. 2016). Winter periods are often typified by highly dissipative beach states (Austin et al., 2010; Poate et al., 2014; Scott et al., 2016; Davidson et al., 2017). The low tide beach gradient is such that tanβ = 0.012, where β is the beach profile slope, and the intertidal beach is relatively flat (tanβ = 0.015-0.025) with a concave-shaped profile. PB sediment is composed of medium quartz sand (d_{50} = 0.35 mm) with a relatively high carbonate content (~50 %) which suggests the influence of offshore sediments (Austin et al., 2010; Poate et al., 2014; Inch et al., 2017) and supply of sediment from the lower shoreface to the beach. PB has a bar system with some rip channels exposed during spring tide low water but is relatively homogenous alongshore and featureless on the upper intertidal (Austin et al., 2010, 2013; Poate et al., 2014; Inch et al., 2017).

The beach system is dominated by cross-shore surf zone driven sediment transport and shore-normal waves (Scott et al., 2016) and the embayment presents important rip circulation. At locations where rip circulation is not active, longshore currents dominate (Austin et al., 2010). Offshore sediment transport has been shown to be dominated by bed return flow currents aided by rip currents during shore-normal storms, which advect sediments from the intertidal upper beach, depositing it in the subtidal sand bars (Scott et al., 2016). Wave-ripples have been shown to develop on the upper shoreface of PB (between 1-6 m depth) under low-energy conditions (orbital velocities < 0.65 m/s) and have been observed to migrate onshore, with a maximum migration rate just onshore of the wave breakpoint (Miles et al., 2014). Onshore ripple migration was shown to correlate with positive (onshore) wave skewness while its direction was dependent on the surf position-controlled velocity skewness, orbital velocity, and mean flow (Miles et al., 2014). Sediment transport rates associated with these bedforms were also onshore directed and increased shoreward which contributed up to the 15% of the total sediment transport (Miles and Thorpe, 2015).

Exchange of sediment between the beach and the lower shoreface occurred at PB during the 2013-2014 winter, the stormiest on record for the Ireland-UK domain over the past 60-years (Masselink et al., 2016; Scott et al., 2016). The sediment eroded from the beach was mainly deposited in large subtidal bar systems, while some were transported offshore (Scott et al., 2016). After the period of storms, beach recovery occurred by migration of bars and nearshore sediment transport onshore (Masselink et al., 2016; Scott et al., 2016). However, part of the sediment eroded from the beach during storms was still retained in the subtidal bar system and remained inactive on the lower shoreface (Scott et al., 2016). Multiannual sediment budgets (Valiente et al.,2019b; 2020) highlighted the importance of lower shoreface sediment transport to sediment budgets of the PB embayment, both in cross-shore and along-shore directions.

3. Methodology

Observations reported here were collected with an instrumented benthic tripod, mini-STABLE (**S**ediment **T**ransport **A**nd **B**oundary **L**ayer Equipment) deployed at approximately 20 m depth referenced to Ordnance Datum Newlyn (ODN) and about 1.5 km offshore of Perranporth Beach (PB) at 5.1646º W 50.3690° N (Fig. 1) from the 18 January to 12 March 2017.

3.1. Study-site geomorphology

The geomorphological setting of the study site was put in context by a Digital Elevation Model (DEM) constructed by combining LIDAR data at 1 m of resolution and multi-beam bathymetry data at 2 m resolution. The DEM was corrected and referenced to Ordnance Datum Newlyn (ODN) using the Vertical Offshore Reference Frame model (VORF) facilitated by the United Kingdom Hydrographic Office and it was imported into a Geographic Information System (ESRI's ArcGIS© desktop v. 10.3). The bathymetry and the topography were displayed using a Universal Transverse Mercator (UTM 30N zone) projection in World Geodetic System (WGS-84) geographic coordinate system and Datum (Fig. 1 b).

3.2. Observational campaign

3.2.1. Bottom sediment samples

Two sediment samples were recovered at the location of the Mini-STABLE deployment site using a Van Veen Grab, during the tripod recovery on the 12 March 2017 (Fig. 1 b). The grabs were subsampled and analysed at Marine Sciences Institute facilities of the Scientific Research Council (CSIC) in Barcelona (Spain). They were first dried in an oven at 80°C for 24 hours. The sediment fraction finer than 2000 µm was examined using an LA-950V2 laser scattering particle size distribution analyser. From the data the grain size distribution and the median gain size, d_{50}, were derived.

3.2.2. Winds and waves

The wave field information was obtained from the Directional Waverider Buoy off Perranporth (Datawell; Directional Waverider MkIII) available online via the Channel Coastal Observatory (www.channelcoast.org). The buoy was located at a water depth of ~20 m referenced to Ordnance Datum Newlyn (Fig. 1 b). Since both the wave buoy and the benthic tripod are deployed in similar depths and close location, it is reasonable to expect that the wave buoy spectra are representative of the benthic tripod location (see location in Fig. 1 b).

3.2.3. Mini-STABLE tripod instrumentation

While the deployed benthic tripod hosted a large number of acoustic and optical instruments, we will focus on data collected by a three-dimensional Acoustic Ripple Profiler 3D-ARP, (http://www.marine-electronics.co.uk/) (Bell and Thorne, 2007; Marine Electronics, 2009; Thorne et al., 2013; Moate et al., 2016; Kramer and Winter, 2016; Thorne et al., 2018), and an Acoustic Doppler Velocimetry (ADV, Nortek Vector).

The 3D-ARP is a dual axis, mechanically rotated, pencil beam scanning sonar operating at 1.1 MHz used to determine how the seabed micro-morphology (< 1 m length scale) evolves with time. Regular scans of a circular area of the seabed allow the relationship between the bed morphology and the changing hydrodynamic conditions to be examined (Thorne and Hanes, 2002; Lichtman et al 2018). The 3D-ARP was clamped to the underside of the frame at a nominal height of 1.2 m above the bottom of the frame. A full bathymetry scan was recorded every 2 hours. With the sensor at ~1.2 metres above the bed, mab, the circular area covered by the scans was ~4 m in diameter. The vertical resolution was 2 mm directly below the transducer (nadir) (Thorne et al., 2018). The bed surface acoustic backscattered data points were gridded into a horizontal resolution of $\Delta x = \Delta y = 5$ mm resulting in a digital elevation map with consistent grid cells.

The ADV was configured into the XYZ coordinate system. A rotation of the axis to earth coordinates was applied using the mean heading angle recorded by the ADV's compass during the first 400 bursts (period of the study). Velocity components were then referenced to the shoreline (11° with respect to the north). The ADV was configured to a sampling rate of 16 Hz and nominal velocity range of 1 m/s. The ADV sampled 12.5 minute bursts every hour. The ADV transducer was located at 1.19 m above the bottom of the frame (see Table I). ADV measurements were verified, tested and processed by applying a quality data control procedure and a despiking method based on Goring and Nikora (2002). A concurrently deployed

Acoustic Doppler Current Profiler (Nortek Signature 1000 AD2CP) is used here to provide the water depth time series at 4 Hz continuously during the whole period of the Mini-STABLE frame deployment (see Table I).

Table 1.- Details of the relevant instruments deployed on the Mini-STABLE frame and of the Perranporth WaveRider buoy. The period analysed was from the 18 January to the 3 February 2017.

Instrument	Measurement used	Sampling interval	Location
ADV	Velocity, intensity and direction	1 h	1.19 mab (Mini-STABLE)
3D-ARP	Seabed micro-bathymetry	2 h	1.2 mab (Mini-STABLE)
AD2CP	Water depth	0.25 s	1.82 mab (Mini-STABLE)
Directional Waverider Buoy	H_s, T_z, T_p	30 min	20 m of water depth (ODN)

3.3. Data Analyses

3.3.1. Seabed detection

The 3D-ARP can be used to record the range at which a threshold backscatter level is encountered for each head position. The data were processed using the bed recognition algorithm suggested by (Bell and Thorne (1997a) which extracts the precise position of the bed echo and obtains the coordinates (x,y,z) of the sea bed for each scan. The method compares the signal with an expected pattern and selects the best match between both (Bell and Thorne, 1997b, Thorne et al 2018). A program was designed to keep running orders applied to detect anomalous points and replace them with estimates based on values from the adjacent space and time bins. In addition, with increasing range from the transducer, the backscattered echo level declines due to signal spherical spreading and scattering in the water column. To reduce noise, the echo signals were smoothed by a five-point window moving average at the bed profile stage after the bed detection. Finally, the seabed topographic variation at the study site was calculated by averaging the z-coordinate of each scan from the 3D-ARP data during the whole period studied (including the periods with the scour formation around the frame legs).

Ripple observations

Ripple geometry and dimensions are here described as the orientation of the crestlines, and the cross-sectional ripple height and wavelength (η and λ, respectively). To determine the spatial variability and the geometric properties of ripples, a method that determined the locations of the crests and troughs in a measured bed elevation profile was needed and then, the geometric properties of individual ripples were determined. The ripple dimensions were estimated from the small-scale gridded bathymetry dataset from the 3D-ARP as follow: (i) the central area of the scans was cropped considering only a square of 0.6 x 0.6 m (the points directly below the transducer or nadir angle are where scans provide the best resolution) and also to remove or minimise scour (Fig. 2 a and b). (ii) The global trend was subtracted from the bathymetry in order to focus only on the fluctuations of the seabed elevations around a horizontal reference level ignoring other morphologies not related to the ripples (Fig. 2 c and d). A fifth order polynomial based on least squares was removed profile by profile (swath by swath) at each scan. The resulting residual bathymetry is a zero-mean bathymetry. (iii) The crest orientation of the ripples was considered by selecting the direction which ripples crests were closer (the smallest wavelength). Therefore, a first approximation for ripple wavelengths was estimated by using the transect method which evaluates for the local extrema (crest or trough) between zero down-crossings and the measured distance between them. (iv) The scans were rotated perpendicular to the ripple crests-lines. Ripple crests were detected for each profile or transect. (v) The ripple height was estimated statistically using the standard deviation of the elevation multiplied by a factor equal to $2\sqrt{2}$ (Traykovski et al., 1999, Thorne et al 2009). (vi) Ripple wavelength was estimated again by using the same transect method but now considering transects perpendicular to the ripple crests. A smooth window was applied to each transect and wavelengths larger than 40 cm were removed as these were considered larger seabed undulations or irregularities and not related to ripples. Finally, the mean wavelengths for each transect and for each scan, were calculated.

Ripple migration was analysed by using 2D cross-correlation method, which accounts for tidal rotation and wave forcing at different angles (Lichtman et al., 2018). The migration distances were calculated from spatial difference between successive (2-hourly) 3D-ARP bed scans, determined by 2D cross-correlation. The distance of migration between two scans divided by the 120 minutes gave the migration rate. The area used for the 2D cross-correlation was the same square of 0.6 x 0.6 m as used for ripple morphology analysis (Fig. 2).

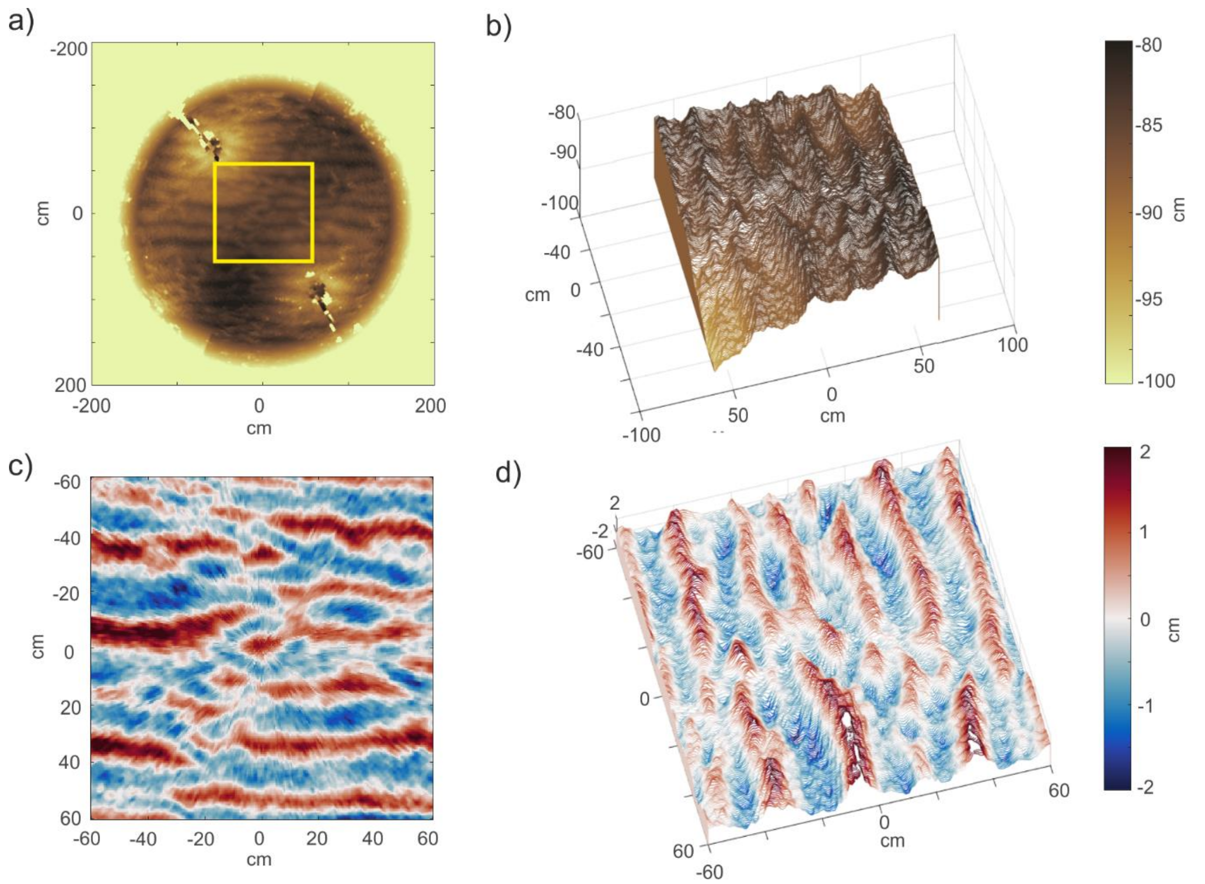

Figure 2.- Example of the pre-processing applied automatically to each scan before ripple dimensions analysis using cmocean colormaps (Thyng et al., 2016): (a) complete scan measured with the 3D-ARP on the 31st of January at 0 h, the yellow square at the centre is the cropped area of 0.6 x 0.6 m. The two black lines are two of the tripod legs (some scour around them is visible); (b) three-dimensional view of the cropped area; (c) zero-mean residual bathymetry after subtract the global trend; (d) three-dimensional view of c). Note that a) and b) scale are distance from 3D-ARP to seabed and c) and d) scale are seabed topography variations.

The influence of scour

Over the time the frame was deployed, the benthic tripod did induce scour around the legs (Fig. 2). Since the alteration by the frame of the near-bottom hydrodynamics as well as the seabed morphology can modify the processes related to ripple formation and dynamism, the ripple analysis was focused only on the early part of the record prior to significant scouring to retain the integrity of the data analysis. The period analysed was from the 18 January to the 3 February 2017, when scour was either not present or was considered to have limited impact on the hydrodynamics and the processes related to ripple formation and evolution.

3.3.2. Hydrodynamic data analysis

The parameters of orbital velocity, wave skewness, seabed roughness, bottom shear stress, Shields parameter and other relationships derived from them, such as ripple predictions and sediment transport rates were estimated from hydrodynamic measurements. Since the methods utilized here are approaches frequently used and well described in the literature, only a short description is presented in this section and the original works are referred for a detailed description of each method.

Wave parameters

Wave spectrum parameters were directly obtained from the directional wave buoy data (Table I) and provided half-hourly time series for the significant wave height (H_s), the zero up-crossing wave period (T_z) defined spectrally, the peak period (T_p); and the peak wave direction (direction of the waves with the highest energy) during the study period. The near-bottom wave orbital velocity, U_w, was then calculated following small-amplitude linear wave theory considering regular waves (Soulsby, 2006; Wiberg and Sherwoord, 2008). This approach is sufficient when the wave height is small compared to the waves wavelength and the water depth and the water is shallow with respect to the wavelength (Wiberg and Sherwood, 2008; Xiong et al., 2018) as was the case at our study site. The Newton-Raphson iteration method was used to determine the wave number k from the dispersion equation following the Fenton and McKee (1990) algorithm.

Wave skewness

The normalized velocity skewness was calculated from ADV measurements. It is defined as (Elgar, 1987):

$$U_{sk} = \frac{\overline{(u(z,t)-\bar{u})^3}}{u_{rms}(z)^3} \quad \text{(eq. 1)}$$

Where $u(z,t)$ is the instantaneous cross-shore horizontal velocity, the overbar denotes time-averaging over a 12.5 minute burst of the ADV data (sampling at 16 Hz), and z is at the depth of measurements.

$$u_{rms}(z) = \overline{(u(z,t)-\bar{u})^2}^{1/2} \quad \text{(eq. 2)}$$

Seabed roughness

The total roughness length (z_0) is the sum of the roughness due to grain size (z_{0s}), the form-drag roughness (z_{0f}) and the sediment transport component of roughness (z_{0t}) (Soulsby 1997):

$$z_{0s} = 2.5d_{50}/30 = d_{50}/12 \quad \text{(eq. 3)}$$

$$z_{0f} = a_r \frac{\eta^2}{\lambda} \quad \text{(eq. 4)}$$

$$z_{0tc} = \frac{5\tau_{0s}}{30g(\rho_s-\rho)} \quad \text{for currents} \quad \text{(eq. 5)}$$

$$z_{0tw} = 0.00533 \cdot {U_w}^{2.25} \quad \text{for waves} \quad \text{(eq. 6)}$$

Where τ_{0s} is the skin-friction shear stress according to Soulsby (1997) (see eq. 10 below), and a_r is an empirical coefficient a_r =0.533 according to Raudkivi (1988), η and λ are the ripple height and wavelength, respectively; U_w is the wave orbital velocity; d_{50} is the median sediment grain size; g is the acceleration due to gravity; ρ is the water density; and ρ_s is the sediment density.

Because ripples were arranged parallel to the near-bottom currents at our study site (see results), the form-drag roughness effect was considered negligible for the currents parameters analysis resulting in a total roughness length as follows:

$$z_{0c} = z_{0s} + z_{0tc} \quad \text{for currents} \quad \text{(eq. 7)}$$

$$z_{0w} = z_{0s} + z_{0f} + z_{0tw} \quad \text{for waves} \quad \text{(eq. 8)}$$

Bed shear stress

Bed shear stresses are calculated using the model for combined waves and currents proposed by Soulsby and Clarke (2005), and modified by Malarkey and Davies (2012). This model includes a representation of non-linear wave-current interactions and is applicable to hydrodynamically rough beds under the approximation of $z_0 << BL << h$ where z_0 is the bed roughness length, h is the water depth, and BL is the wave boundary layer thickness calculated as $BL = \max\,(a_r\sqrt{0.5 f_w} a_w, z_{0w})$. The wave orbital amplitude, a_w, and wave-only friction factor, f_w, are given by the formulations: $a_w = \frac{U_w T}{2\pi}$ and $f_w = 1.39(a_w/z_{0w})^{-0.52}$. The mean bed shear stress due to combined flow (τ_m), including wave-current interaction, over hydrodynamic rough beds (sand and gravel beds) is:

$$\tau_m = \rho {u_{*m}}^2 \qquad \text{(eq. 9)}$$

where, $u_{*m} = \sqrt{\left[\frac{bu_{*e}}{2a}\right]^2 + \frac{\bar{U}u_{*e}}{a}} - \frac{bu_{*e}}{2a}$; $\bar{U}$ is the depth averaged current speed, calculated from the burst-averaged ADV-measured velocities following Malarkey and Davies (2012); $a = \kappa^{-1} log(\delta/z_0)$, δ is the bottom boundary layer thickness, $b = \kappa^{-1} log(h/e\delta)$, κ =0.4 the von Kármán constant and $u_{*e} = (\frac{\tau_e}{\rho})^{1/2}$ is the effective friction velocity where $\tau_e = \sqrt{{\tau_c}^2 + 2\tau_c\tau_w|cos\phi| + {\tau_w}^2}$. Where ϕ is the angle between the current direction and the wave propagation direction, and τ_c and τ_w are the bed shear stress considering currents alone and waves alone, respectively, estimated as:

$$\tau_c = \rho C_D \bar{U}^2 \qquad \text{(eq. 10)}$$

where C_D is the drag coefficient defined as:

$$C_D = \left[\frac{0.40}{\ln\left(\frac{h}{z_{0c}}\right) - 1}\right]^2 \qquad \text{(eq. 11)}$$

For a sinusoidal wave of period T, and orbital velocity U_w, the amplitude of the bed shear stress is given by:

$$\tau_w = \frac{1}{2}\rho f_w {U_w}^2 \qquad \text{(eq. 12)}$$

The maximum bed shear stress due to combined flow, including wave-current interaction, (Soulsby, 1997) is:

$$\tau_{max} = \left[{\tau_m}^2 (1 + \varepsilon_1 + \varepsilon_2) + {\tau_p}^2 + 2\tau_m \tau_p \sqrt{1 + \varepsilon_1 + \varepsilon_2} |cos\phi| \right]^{1/2} \qquad \text{(eq. 13)}$$

Where $\tau_p = \rho u_{*e} u_{*w}$, see (Soulsby 1983), $\varepsilon_1 = \tau_c \tau_w |cos\phi| / (\tau_c + \tau_w)^2$ and $\varepsilon_2 = {\tau_w}^2 / 4(\tau_c + \tau_w)^2$ and $\tau_w = \rho {u_{*w}}^2$.

Shields parameter and its thresholds

The Shields parameter, θ, is a non-dimensional bed-shear stress variable used to identify or determine when seabed states typically reach the initiation of sediment motion in a fluid flow. The Shields parameter also gives an approximation of the limits of seabed morpho-states in relation to the incident hydrodynamic conditions, in our case for a constant sediment size throughout the study period and evaluated during waves and currents separately (Soulsby et al., 2012).

$$\theta = \frac{\tau}{g(\rho_s - \rho) d_{50}} \qquad \text{(eq. 14)}$$

Where the Shields parameter due to waves (θ_w) and currents (θ_c) are calculated using the equations of τ_w and τ_c defined in eq. 12 and eq.10, respectively.

Shields parameters provide criteria for the definition of thresholds of initiation of movement, wash out and sheet flow regime. The critical Shields parameter for initiation of motion, θ_{cr} is given as (Soulsby 1997)

$$\theta_{cr} = \frac{\tau_{cr}}{g(\rho_s - \rho) d_{50}} = \frac{0.3}{(1 + 1.2D*)} + 0.055[1 - exp(-0.02D^*)] \qquad \text{(eq. 15)}$$

where τ_{cr} is the critical threshold for the bed shear stress; $D^* = d_{50}[(s-1)g/v^2]^{1/3}$ is the dimensionless sediment grain size, with $D^* = 6.64$ at our Perranporth lower shoreface site; $\upsilon = 10^{-6}$ (m^2/s) is the kinematic viscosity coefficient; and $g = 9.81$ (m/s^2) is the gravity acceleration.

According to Soulsby et al. (2012), the limit of wash-out (θ_{wo}) and skin-friction sheet flow threshold (θ_{sf}) can be inferred using a criterion given in terms of skin friction Shields parameters as a function of D*:

$$\theta_{wo} = 1.66{D_*}^{-1.3} \qquad \text{when } D^* > 1.58 \qquad \text{(eq. 16)}$$

$$\theta_{sf} = 2.26 D_*^{-1.3} \qquad \text{when } D^* > 1.58 \qquad \text{(eq. 17)}$$

Ripple prediction

Ripple characteristics are predicted following the equilibrium dimensions of Soulsby et al. (2012), which are based on extensive field and laboratory data sets. This simpler approach is preferred to the non-equilibrium procedure because in the field it is difficult to know the history of development or even a starting point of ripples, so equilibrium can be useful with the proviso that relict ripples can be retained for certain conditions. Following this method, different morpho-states are expected to develop under different hydrodynamic forcing regime, and the method estimates wavelength, λ, and ripple height, η, (from the slope, η / λ) as a function of the hydrodynamic forcing regime and the dominance of waves or currents. The hydrodynamic forcing regimes are here determined by thresholds on the Shields parameter. Ripples only start to evolve above the threshold of initiation of sediment motion (θ_{cr}), which is evaluated as a function of sediment size. Above this limit, ripples grow towards morphologies in equilibrium with the hydrodynamic forcing (Soulsby et al., 2012). For increasing hydrodynamic forcing, ripple dimensions reduce above a wash-out threshold ($\theta > \theta_{wo}$), and disappear above a sheet flow threshold ($\theta > \theta_{sf}$) since θ_{sf} borders the limit of ripple existence (Carmenen, 2009)

Dominance of waves or currents is assessed from the values of θ_w and θ_c. When waves dominate ($\theta_w > \theta_c$), estimated ripple dimensions increase (decrease) with increasing (decreasing) energy due to their functional relationship with the wave orbital velocity. When $\theta_w > \theta_{cr}$ ripples heights, η, and wavelengths, λ, are defined as (Soulsby et al., 2012):

$$\frac{\lambda}{a_w} = [1 + 1.87 \times 10^{-3}\Delta(1 - exp\{-(2 \times 10^{-4}\Delta)^{1.5}\})]^{-1} \qquad \text{(eq. 18)}$$

$$\frac{\eta}{\lambda} = 0.15[1 - exp\{-(5000/\Delta)^{3.5}\}] \qquad \text{(eq. 19)}$$

where $\Delta = a_w/d_{50}$

Otherwise, λ and η are taken as the pre-existing values (relict ripples).

When currents dominate ($\theta_c > \theta_w$) and $\theta_c > \theta_{cr}$ current ripples can develop. For a given grain size, ripples of constant height and wavelength develop if the current speed is maintained for a sufficient period of time, then:

$$\eta_{max} = d_{50} 202\, D^{*-0.554} \qquad \text{for } 1.2 < D^* < 16 \qquad \text{(eq. 20)}$$

$$\lambda_{max} = d_{50}\left(500 + 1881 D^{*-1.5}\right) \qquad \text{for } 1.2 < D^* < 16 \qquad \text{(eq. 21)}$$

Soulsby et al. (2012) defined a reduction in ripple height between θ_{wo} and θ_{sf} assuming that the wavelength is unaffected by wash-out and is equivalent to the maximum value indicated above. Then, the equilibrium ripple height including wash-out is:

$$\begin{cases} \eta_{eq} = \text{ pre} - \text{existing value (relict or frozen ripples)} & 0 < \theta_c < \theta_{cr} \\ \eta_{eq} = \eta_{max} & \theta_{cr} < \theta_c < \theta_{wo} \\ \eta_{eq} = \eta_{max}\left(\frac{\theta_{sf} - \theta_c}{\theta_{sf} - \theta_{wo}}\right) & \theta_{wo} < \theta_c < \theta_{sf} \\ \eta_{eq} = 0 & \theta_c > \theta_{sf} \end{cases} \qquad \text{(eq. 22)}$$

One implication of the method as described above is that the reduction of ripple dimensions for large hydrodynamic forcing is only ensured for current-dominated conditions. Under wave dominance, no reduction is applied to ripple dimensions: ripple wash-out and disappearance under wave sheet flow are therefore not considered (Camenen, 2009; Soulsby et al., 2012). Finally, for waves and currents acting together, this ripple prediction model assumes that only the dominant ripple forcing of the two is present at any time (Li and Amos, 1998).

Sediment transport rate

A semi-quantitative approach to calculate the sediment transport intensity under varying hydrodynamic conditions is applied using rate estimates of van Rijn (2007a, 2007b). This estimation for bedload and suspended sediment load transport uses hydrodynamic conditions (depth, current velocity, wave height, wave period, etc.) as well as sediment size (d_{50}). This method represents a strong simplification of sediment transport processes, although it has shown reasonable veracity for steady and oscillatory flow outside the surf zone with medium-coarse sands (> 200 microns).

To calculate the net sediment trasnport rates (over a wave period), the sum of the bedload (q_b) and suspended load (q_s) transport rates is give by:

$$q_{total} = q_b + q_s \quad \text{(eq. 23)}$$

For coastal flow (steady flow with or without waves) the bedload transport according to van Rijn (2007a) is defined as:

$$q_b = \alpha_b \rho_s U h (d_{50}/h)^{1.2} {M_e}^{1.5} \quad \text{(eq. 24)}$$

Where q_b is the bedload trasnport rate (in kg/s/m); α_b= 0.015; $M_e = (U_e - U_{cr})/[(s-1)gd_{50}]^{0.5}$ is the non-dimensional mobility parameter; $U_e = U + \gamma U_w$ the effective velocity (in m/s) with γ =0.4 for irregular waves; U is the depth averaged flow velocity (m/s); U_w is the orbital velocity (m/s); $U_{cr} = \beta u_{cr,c} + (1-\beta) u_{cr,w}$ is the critical velocity (m/s) with $\beta = U/(U + U_w)$; $u_{cr,c}$ is the critical velocity (m/s) for currents based on Shields; $u_{cr,w}$ is the critical velocity (m/s) for waves, which for the case when 0.00005< $d_{50} < 0.0005$ m, are:

$$u_{cr,c} = 0.19 {d_{50}}^{0.1} \log(12h/3d_{90}) \quad \text{(eq. 25)}$$

$$u_{cr,w} = 0.24[(s-1)g]^{0.66} {d_{50}}^{0.33} {T_p}^{0.33} \quad \text{(eq. 26)}$$

d_{90} is the particle size such the 90% are less or equal (m), and $s = \rho_s/\rho_w$ is the relative density.

The suspended load transport rate is defined as transport of sediment by the mean current while including the effects of wave stirring on the suspended load (van Rijn, 2007b):

$$q_s = 0.012 \rho_s U d_{50} {M_e}^{2.4} D^{*-0.6} \quad \text{(eq. 27)}$$

4. Results

4.1. Shoreface morphology and sediment characteristics

Perranporth shoreface displays a cross-shore profile with slopes of tanβ~ 0.004 and concave-shaped until ~30 m depth (ODN) (Fig. 1 b). Over this area, the seafloor morphology is uniform and homogeneous, limited by rocky outcrops at the north and south ends of the embayment following the emerged cliffs of Devonian rocks (Fig. 1 b). Just at the south of the northern outcrops, at approximately 25 m depth, six subaqueous dunes lie with ~0.5 m high and ~110 m of wavelength, they display asymmetries with the lee side facing to the south, suggesting a dominant southward residual current. At approximately 30 m depth contour (ODN) an abrupt edge 1 m high appears breaking the seafloor homogeneity. It is arranged mainly parallel to the shoreline except at the southern area where the edge appears shallower without apparently any alignment. Offshore of this edge the seafloor changes to more complex morphologies exhibiting tidal channels aligned northeast-southwest, 0.3-0.5 m deep (maximum ~1 m) and widths ranging from tens to hundreds of meters. The head of these channels are located near the rocky outcrops at the north area of the continental shelf, becoming wider towards the southwest. Thus, the study site is in the transitional zone between the tidal morphologies (less than 30 m depth) and the nearshore bars (greater than 6 m depth) on the upper shoreface.

The grain size analyses of the surficial sediment showed a moderately sorted medium sand composition with d_{50} of 266 μm at the Mini-STABLE frame location. 97% of the sediment was sand with 7.6% coarse sand (2 mm > d_{50} > 0.5 mm), 48.1% medium sand (0.5 > d_{50} > 0.25 mm), 36.5% fine sand (0.25 > d_{50} > 0.125 mm), and 4.8% very fine sand (0.125 > d_{50} > 0.063 mm), and the remaining 3% was silt (d_{50} < 0.63 mm) fraction (Fig. 3).

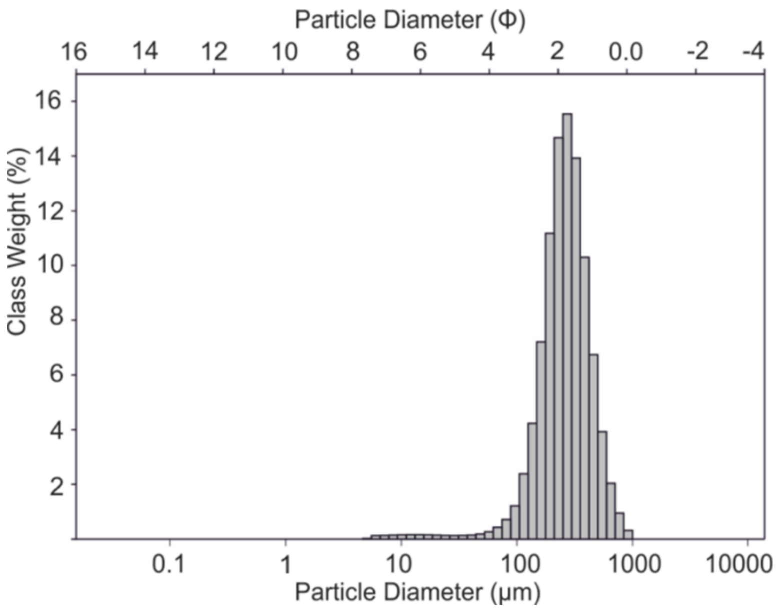

Figure 3.- Grain size distribution of the bottom sediment sample recovered at the Mini-STABLE frame location deployment using the Van Veen Grab during the tripod recovery.

4.2. Time series

4.2.1. Wave conditions

The wave time series shows the root mean square wave height, $H_{rms}\left(H_{rms} = H_s/\sqrt{2}\right)$ ranging from 0.5 m to 2 m and mean wave periods (T_z) from 5 to 10 s (Fig. 4 a). The highest waves (H_{rms} ~ 3 m) took place on 3 February when T_z was between 8-10 s. Wave directions were unidirectional coming from the west-northwest with a mean wave direction of ~280° (data not shown).

The near-bottom wave orbital velocities (U_w) ranged between 0.1 and 0.4 m/s displaying peaks following a similar form to the wave heights time series (Fig. 4b). The highest waves occurred at the end of the period on the 3 February, with orbital velocities increasing to 0.6 m/s.

4.2.2. Water level and currents

Water levels display dominant semi-diurnal tides with strong spring-neap modulation (Fig. 4 c): minimum neap tidal amplitudes were approximately 2.5 m and the maximum spring amplitudes reached approximately 6.3 m. The direction of the near-bed tidal current indicate flood flowing towards north-northeast and ebb towards south (Fig. 4 c). The gradual shift in direction suggests a rotational behaviour and the presence of a near-bed tidal ellipse. The near-bed current magnitude peaked at approximately 0.2 m/s during ebbs and floods (Fig. 4b) with slight flood dominance, indicating a probable northward near-bed residual current at this location.

4.2.3. Near-bottom shear stress

The hydrodynamic forcing acting on the seabed during the study period is characterized by the near-bed shear stress. The stress is presented as the maximum combined wave and current shear stress (τ_{max}), shear stress considering only waves input (τ_w) and shear stress from currents alone (τ_c) (Fig. 4 d). The maximum contributor to the combined wave and currents shear stress was clearly waves, only being reached and seldom exceeded by the current stress during short periods when the orbital velocities were weak < 0.1 m/s (H_{rms} ~ 0.5 m). The combined wave-current shear stress ranged from less than 0.1 to greater than 3 Nm^{-2} over the studied period, with several peaks of τ_{max} > 2 Nm^{-2} and even τ_{max} ~ 4 Nm^{-2} (Fig. 4 d).

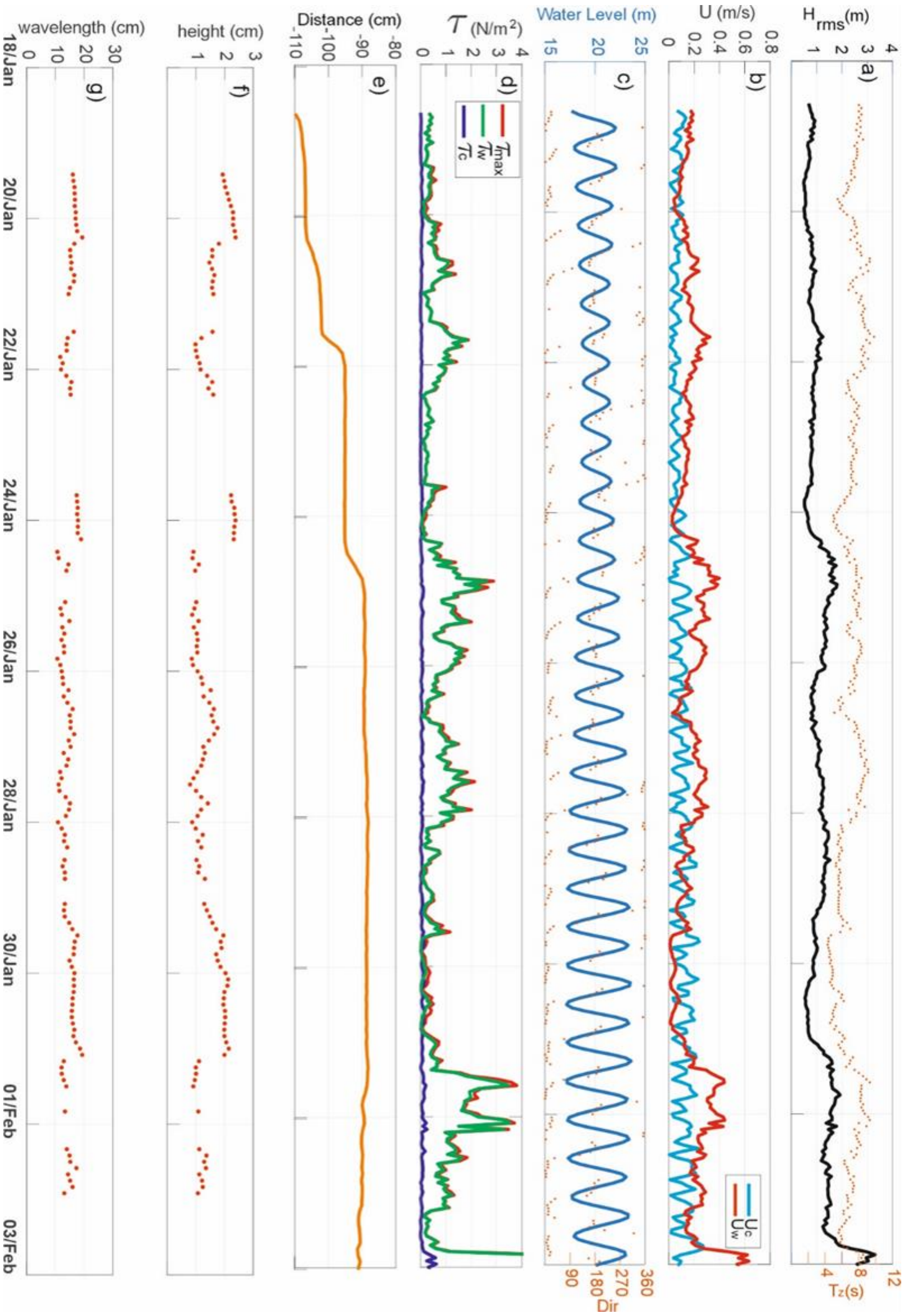

Figure 4.- Time series from the 18 January to 3 February 2017 of: (a) root mean square wave height (H_{rms}) (line) and mean period (T_z) (dots); (b) orbital velocity (red line) and current speed from ADV (blue line); (c) water level depth (line) and direction of near-bed tidal current (dots); (d) maximum combined wave and currents shear stress (red line); wave-alone shear stress (green line), and current-alone mean shear stress (blue line); (e) depth-averaged bed level displaying the relative distance between the 3D-ARP transducer and the seabed level; (f) observed ripple height; (g) observed ripple wavelength.

4.2.4. Mean bed level variations

The topographic variations of the bed level from the 18 January to 3 February show that the frame experienced four discrete events of rapid settling during the first week of deployment (before approximately 25 January), as evidenced by the steep gradient in the distance between the 3D-ARP transducer and the seabed (Fig. 4e).

The first event occurred on the 18 January 2017 with 2.6 cm of sinking and was probably due to initial settling of the frame following deployment. Subsequent settling periods appear to be associated with increased wave activity and occurred 20, 21 and 24 January with settling of 4.2 cm, 7 cm and 5.9 cm respectively. Each of these periods lasted around 16 h and seemed to be a consequence of the frame accommodation and sinking because of its own weight. The association with increased wave activity is likely to result from increased wave-induced pore pressure and resulting liquefaction of the seabed. The overall settling was ~20 cm (Fig. 4 e). After the 25 January, the bed level remained more or less constant without significant changes apart from a small increase of the seabed-to-transducer distance occurring between 31 January and 3 February.

4.2.5. Ripple observations and dynamics

The presence of ripples on the Perranporth lower shoreface seabed from the 18 January to 3 February 2017 was the most common situation, occurring ~64% of the time (Fig. 4 f, g). Ripple crestlines were aligned in a north-south direction, nearly parallel to the coastline (which is ~11º to North). Most ripple crestlines were oriented almost perpendicular to the wave direction approach (west-east) and parallel to the dominant current direction (north-south). Thus, ripple occurrence was mainly related to wave action. The orientation of the ripples also has important implications for the bed roughness that is effectively felt by the flow: in particular, the ripple-induced roughness (eq. 4) associated with the 2D wave ripples observed here is unlikely to affect the roughness felt by tidal currents, which primarily flows along ripple crests. Ripple morphology ranged from 2D to 3D, smaller ripples with sinusoidal or curved crests (Fig. 5 a and b, respectively). During periods when ripples were not observed (gaps in the data in Figure 4 f, g), the scans displayed a flat bed and on occasions seabed morphologies with a zig-zag pattern. These patterns, show complex seabed morphologies and ripple coalescence (Rousseaux 2006). Because of their uncertain interpretation, they were discarded from the present analysis. The development of 2D and 3D ripples occurred during ~19% and ~45% of the time studied, respectively (Fig. 6 a, b). In general, 2D ripples displayed heights up to 2 cm and wavelengths ~15-20 cm, while 3D ripples displayed slightly lower heights ~1-1.5 cm and wavelengths ~10-15 cm (Fig. 6 a, b).

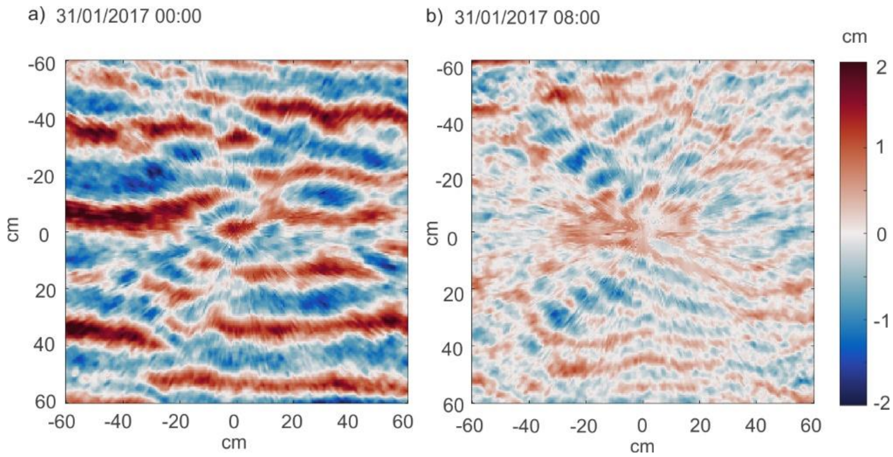

Figure 5.- Examples of 3D-ARP images for using cmocean colormaps (Thyng et al., 2016): (a) 2D ripple morphologies with bigger dimensions and rectilinear crests (31/01/2017 0h) and (b) 3D ripple morphologies with smaller dimensions and sinusoidal or curvilinear crests (31/01/2017 8h).

In general, 2D ripples occurred under low-energy wave conditions (H_{rms} < 1 m and T_z < 8 s) (orbital velocities < 0.2 m/s) and tidal currents lower than 0.2 m/s. Under increasingly energetic conditions, 2D ripples slightly increased their dimensions until a maximum size (~2.4 cm height and ~19.5 cm wavelength, see for example around 20 January). Beyond these conditions, ripple size dropped significantly corresponding with a transition from 2D to 3D ripple, which is interpreted as ripple degradation when ripple wash-out conditions were reached (Fig. 6, 20 - 21 January, 24 January). Observations also showed gradation from 2D to 3D ripples to flat bottom with increasing bottom shear stress (Fig. 6, 24-25 January, 31 January).

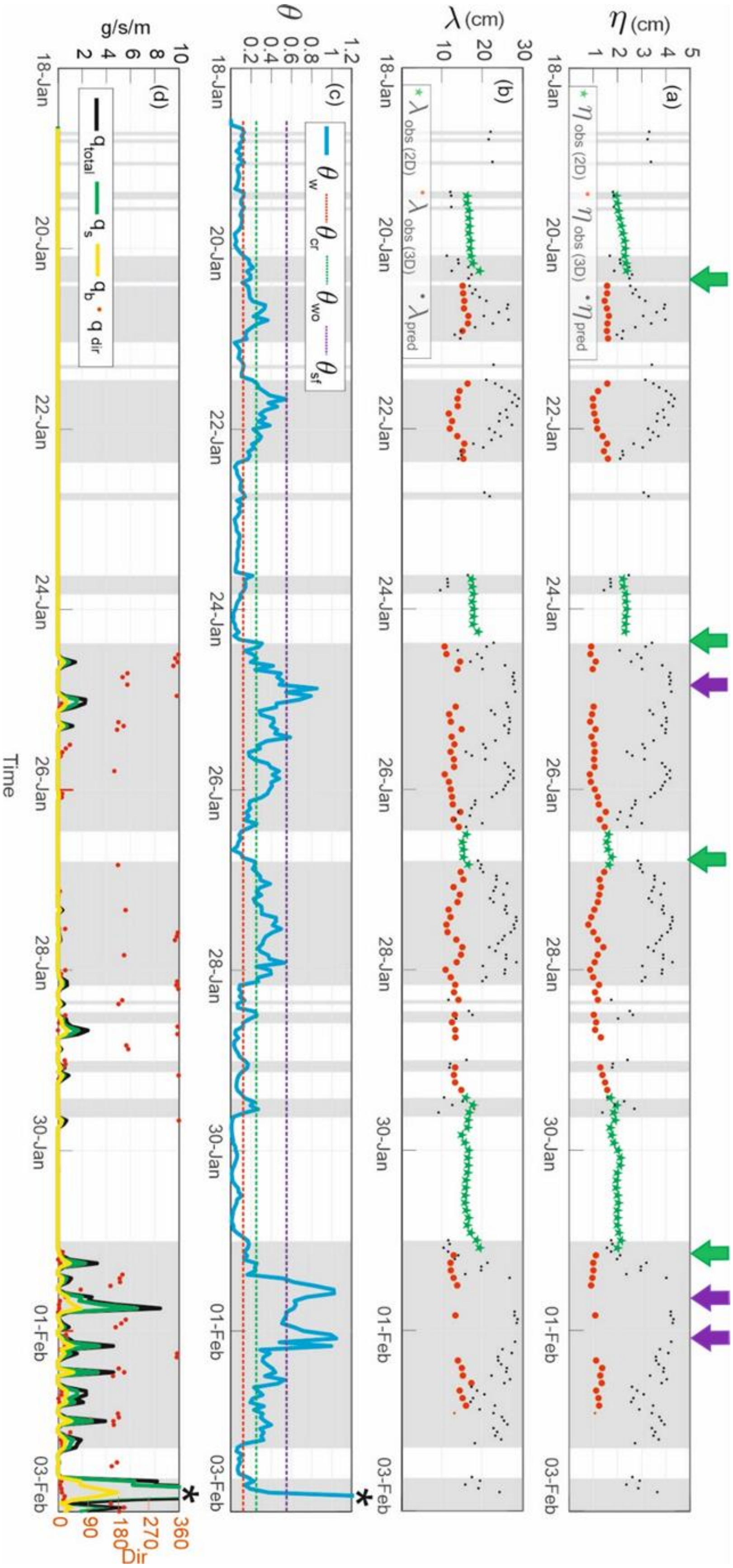
(a)
η (cm)
$\eta_{obs\,(2D)}$ $\eta_{obs\,(3D)}$ η_{pred}
(b)
λ (cm)
$\lambda_{obs\,(2D)}$ $\lambda_{obs\,(3D)}$ λ_{pred}
(c)
θ
θ_w θ_{cr} θ_{wo} θ_{sf}
(d)
g/s/m
q_{total} q_s q_b q_{dir}
Dir
Time
18-Jan
20-Jan
22-Jan
24-Jan
26-Jan
28-Jan
30-Jan
01-Feb
03-Feb

Figure 6.- Time series of (a) ripple height and (b) ripple wavelength showing observed 3D (red dots) and 2D (green stars) ripples and predictions (black dots) from Soulsby et al (2012), eq. (19 and 18); (c) Shield parameter due to waves (θ_w, eq (10)) (Shield caused by currents is very low and is not represented), and threshold of motion (θ_{cr}, eq (12)), wash-out (θ_{wo}, eq (13)), and sheet flow (θ_{sf}, eq (14)); and (d) total sediment transport (eq. (23)), suspended load sediment transport (eq. (27)), bed load sediment transport (eq. (24)) and resultant sediment transport direction with respect to north where 0 and 360 degrees are northward direction (red dots and right vertical axis). (* data out of range). Shaded areas indicate periods when Shields parameter exceeded the threshold of sediment motion. Ripple observations in unshaded areas can correspond to relict ripples whereas plane bed in shaded areas is interpreted as sheet flow conditions. Arrows on top of the figure highlights transitions between 2D and 3D ripples (green) and between 3D ripples and plane bed (sheet flow conditions) (purple).

The outcome from the migration analysis was somewhat inconclusive. In addition, no ripple migration was visually observed from the scans. No measurable ripple migration was detected during the study period. Based on observations of the seabed morphology, scans from the 3D-ARP indicated the 2D ripples were stationary while 3D ripples sometimes exhibited some dynamism by changing the crests curvature between two successive scans which indicated readjustment of these bedforms rather than migration in a specific direction.

4.2.6 <u>Observations and estimated Shields parameters thresholds</u>

In order to estimate thresholds of initiation of sediment motion, the Shields parameter due to waves and currents was calculated using the methodology previously described (Fig. 6 c). As expected, the time evolution of the wave Shields parameter is similar to that of the wave shear stress and the orbital velocities and values reach in excess of 0.8. The Shields parameter for current only conditions was almost negligible remaining below the sediment motion threshold during the whole period and is therefore not plotted.

In addition, thresholds for the wave Shields parameters were established based on the concurrent observations of ripple development, degradation and disappearance from the time series of the 3D-ARP data. These values were taken as the threshold values for starting ripple formation ($\theta_{cr} = 0.12$) (vortex ripple), ripple wash-out ($\theta_{wo} = 0.25$) (transition from 2D to 3D ripples) and sheet flow ($\theta_{sf} = 0.55$) regimes based on our time series observations (see Fig. 6). These values roughly correspond with peak values suggested by Thorne et al. (2009) for bedform characteristics under different boundary layer flow conditions (< 0.2, 0.2-0.7 and >0.7 for 2D ripples, transition ripples and dynamically plane bed respectively). They are also larger than the values obtained using equations 15-17. Such discrepancies between Shields thresholds and observations of ripple development and disappearance have also been previously reported (e.g. Bagnold, 1946; Hanes et al., 2001; Camenen, 2009). These differences can be a consequence of the strong simplifications involved in calculations (e.g. d_{50} as the representative sediment size, the lack of a uniform sediment grain size, and the complexities of bottom boundary layer dynamics, etc.) (Traykovski et al., 1999). This also impacts the prediction of ripple dimensions since predictors (e.g. equations 18 to 22 here) rely on these threshold values. We therefore used our empirical thresholds instead of the values from equations 15-17 in the predictions of ripple dimensions (black points in Fig. 6 a and b).

The thresholds extracted from our time series suggest that hydrodynamic forcing remained below the threshold of sediment motion at our study site on the Perranporth lower shoreface during ~38% the study period. The rest of the time (62%) hydrodynamic (wave) forcing was strong enough to exceed the threshold of grain motion. Hydrodynamic conditions were strong enough to be between washout and sheet flow ($\theta_{wo} < \theta_w < \theta_{sf}$) for 30% of the reported time series and exceeded sheet flow threshold for 11% of the reported time series.

4.2.7 Near-bottom sediment transport

During our study period, near-bed hydrodynamics at our study site on the Perranporth lower shoreface were dominated by waves coming from the west with a mean approach angle of ~280° N and north-south currents with slightly rotational component of north-northeast south-southwest corresponding to the flood and ebb tidal flows respectively (Figs. 6 d; 7 a). The sediment transport rates (bedload, suspended load, and total load) estimated from near-bed hydrodynamic observations following equations 23-27 primarily occurred in several peaks typically for relatively energetic conditions during the deployment period (i.e.

24, 25, 26, 27, 28, 29 31 January and 1, 2 February) (Fig. 7 b). The estimated suspended load transport widely dominated over the bed load transport (77.2% and 22.8%, respectively). These results are broadly consistent with the lack of observed ripple migration corresponding to small bedload transport since peaks typically coincide with conditions energetic enough to induce ripple washout or sheet flow. The resulting sediment transport component in east-west direction is almost zero (Fig. 7 b) because of the oscillatory velocity component (in black in Fig. 7 a). The peaks of the sediment transport correspond to north-south (360°-180°, respectively) velocities (Fig. 7 b), with a dominant northern transport (Fig. 7 c).

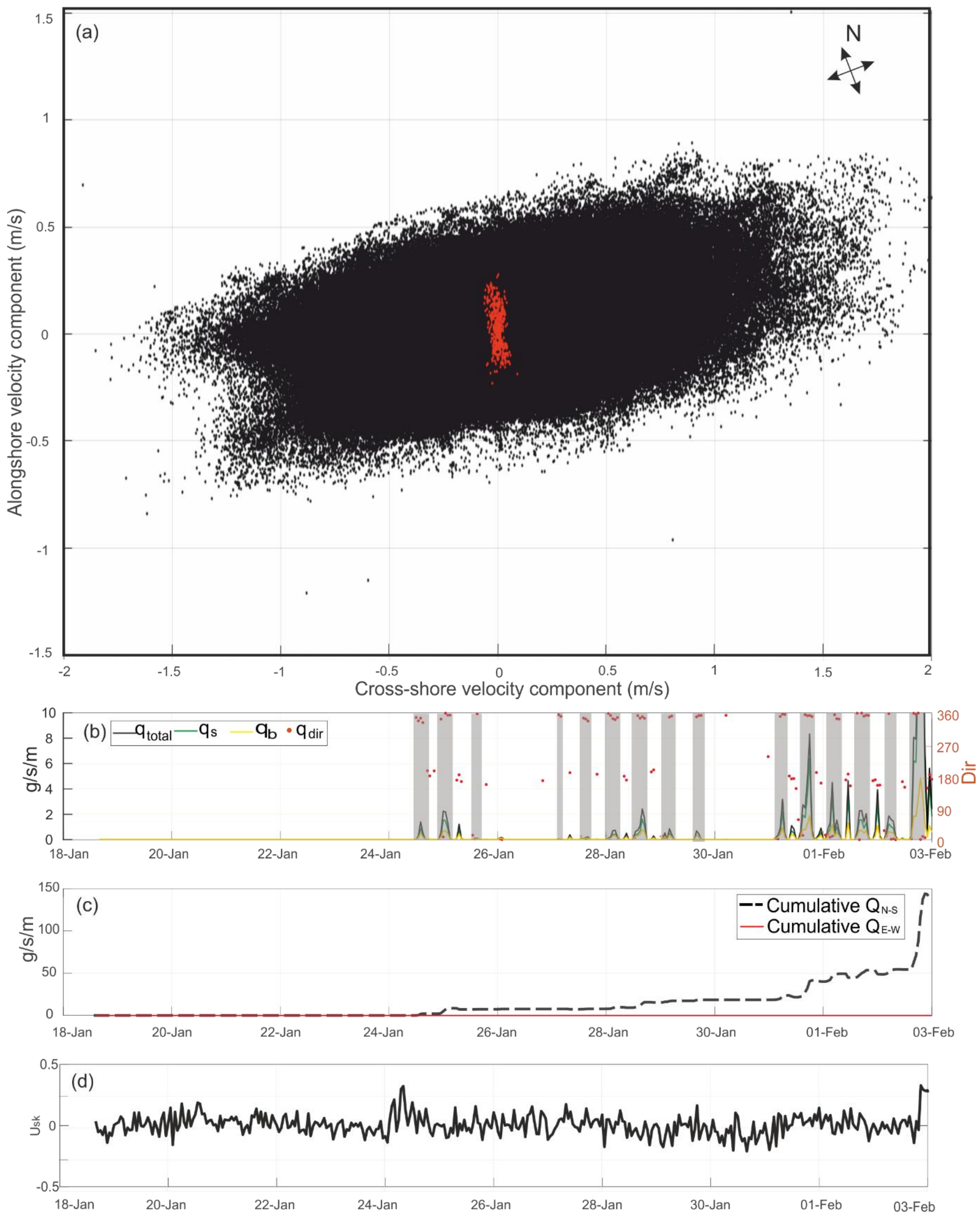
(a)
N
Alongshore velocity component (m/s)
Cross-shore velocity component (m/s)
(b)
q total
q s
q b
q dir
g/s/m
Dir
(c)
Cumulative Q N-S
Cumulative Q E-W
g/s/m
(d)
Usk
18-Jan
20-Jan
22-Jan
24-Jan
26-Jan
28-Jan
30-Jan
01-Feb
03-Feb

Figure 7.- (a) Dispersion diagram of cross-shore velocity components (x axes) and alongshore velocity component (y axes) considering the east (onshore) and north components positive values. Black dots correspond to intra-burst data and red dots the mean-burst data; (b) total sediment transport (blue line), suspended load sediment transport (green line), bed load sediment transport (yellow line) and resultant sediment transport direction (red dots and right vertical axis). Shaded areas show sediment transport episodes towards the north. The maximum peak on February 3rd (>20 g/s/m) is not represented; (c) cumulative sediment transport towards the north-south direction (black line) and towards the east-west direction (red line) considering the north and east directions positive; (d) cross-shore wave velocity skewness.

5. Discussion

5.1. Ripple development, transitions and regimes

In general, the presence of ripples and their morphological changes depend on the flow conditions and the ability of the ripple to adapt to the new hydrodynamic conditions until they reach the equilibrium (Nelson and Voulgaris, 2014). Transitions between 2D, 3D ripples and plane bed conditions in energetically changing conditions as described here for the Perranporth lower shoreface, have also been observed at other sites (Hanes et al., 2001; Nelson and Voulgaris, 2014). But, with energetically variable flow conditions, ripple equilibrium is unlikely to be reached and active changes in ripple height, wavelength, and orientation can be expected. In fact, ripples in flow conditions close to the inception of motion, should be only stable in conditions close to or below the critical value, in this case maintaining relict bedforms (Bagnold, 1946; Camenen, 2009).

Because of the orientation of the ripple crestline with respect to wave propagation and tidal current directions, the ripples we observed on the Perranporth lower shoreface were clearly wave ripples. The absence of current-dominated ripples in our observations is the consequence of the relative low-intensity of the recorded tidal currents during the study period. Two ripple categories were recognized as vortex ripples: 2D ripples with rectilinear crestlines, height, η>2 cm and length, λ=15-20 cm, and 3D ripples with more sinusoidal crestlines, η=1-1.5 cm and λ=10-15 cm. Indeed, the displayed crestline morphology, the steepness value (> 0.1), and the d_0/d_{50} relation (< 5000) are characteristic of vortex ripples (Clifton and Dingler, 1984). Even though the 3D ripples have lower steepness and higher d_0/d_{50} ratio than the 2D ripples, their characteristics still correspond to that of vortex ripples (Clifton and Dingler, 1984).

Observed trends of small scale seabed morphology can be linked to the strength of wave forcing during the study period. For low energy conditions, typically such that the threshold of motion is not reached, the seabed was stable and static. Ripples, when present, displayed close to constant dimensions, suggesting relict ripples (Fig. 6, e.g. 19, 23 -24, 26, 28, 29 -30 January). Interestingly, while ripple development would be expected about the 51% of the study period when $\theta_{cr} < \theta_w < \theta_{sf}$, ripples were observed during 64% of the study period further supporting the presence of relict ripples for significant periods of time. For increasing wave forcing, stationary vortex ripples were generated with changes in size and dimensionality depending on the wave forcing. The transition from larger 2D vortex ripple to the smaller 3D vortex ripples generally was abrupt (see green arrows in Fig. 6) and interpreted as ripple degradation under increasing energetic conditions (exceedance of wash-out threshold), while the reverse transition (small 3D to large 2D) vortex ripples was progressive and typically occurred with decreasing wave energy (Fig. 6, e.g. 25-27 January,). For the highest energy conditions, ripples disappeared when the Shields parameter surpass the sheet flow threshold (purple arrows in Fig. 6). Under these intense conditions, scour started to form on the seabed around the legs of the deployed instrument frame, consistent with previous results showing scour increasing with hydrodynamic forcing (Bolaños et al., 2011).

5.2. Comparison with ripple predictor

Since waves largely dominated near-bed hydrodynamics and the current Shields parameter was consistently below the threshold of motion during the study period (Fig. 6 c), we only applied the formulation for wave-generated ripples, using Shields parameter thresholds determined empirically from our time series. The presence of ripples versus flat bed conditions are well reproduced with erroneous predictions of 2D vortex ripples instead of flat bed only occurring twice on the 18 and 22 January (Fig. 6 a and b). Such an outcome is likely to be a consequence of using empirically determined thresholds rather than validation of the general predictor and highlights the importance of accurate estimates of these thresholds.

Predictions of 2D ripple dimensions are satisfactory under low energy conditions, but ripples dimensions are poorly predicted under several other conditions. Under low energy conditions ($\theta < \theta_{cr}$) a flat bed is predicted from the model, but ripples were observed and interpreted as relict ripples during approximately 10% of the time during the reported study period on the Perranporth lower shoreface (Fig. 6, e.g. 24 January). From the comparison with the observed ripples, predictions for low energy conditions appear to be particularly challenging because our observations do not consistently report constant ripple dimensions (relict ripples) for each period below the threshold of motion (see unshaded sections in Fig. 6).

Predictions of 3D ripple dimensions systematically and significantly overestimate observations. The predictor also results in larger variability in both height and wavelength than the observations, with η between 2 and 4.5 cm and λ between 15 and 30 cm (Fig. 6 a and b). The explanation for these large discrepancies is relatively simple in that the predictor used here (Soulsby et al., 2012) does not account for the reduction of ripple dimensions above the washout threshold for wave-generated ripples. Similar results were obtained in other studies under wash-out conditions (Hanes et al., 2001; Camenen, 2009; Soulsby et al., 2012) and highlight an important deficiency of such a wave ripple predictor.

5.3. Contribution to embayment sediment pathways and budgets

The estimated dominant near-bottom sediment transport direction was close to alongshore and almost parallel to the ripple crestlines, switching between north and south following the ebbs and floods tidal flows (red dots in Figs. 7 a, b) but with a clear net transport northward owing to the flood dominance of the near-bed tidal currents at this location (Fig. 7 c). This pattern is likely the result of sediment resuspension by wave stirring and subsequent transport due to tidal currents, which is characteristic in environments dominated by combined waves and currents (Traykovski et al., 1999; van Rijn, 2007a, 2007b). Sediment transport mostly occurring along ripple crestlines also explains the observed changes in the morphology of the 3D ripples (mostly ripple crest realignment) until higher energetic regimes completely washed-out to result in sheet flow conditions. These seabed modifications and ripple dynamics occurred relatively rapidly according to 3D-ARP observations with ripple reorientation between 2 consecutive scans two hours apart.

An important consequence of the orientation of the coast in this specific location is that the predicted net northward sediment flux results in both longshore and (smaller) offshore components. While this is consistent with measured alongshore and offshore burst averaged currents, further observational evidence of sediment fluxes would be necessary for complete confirmation. The inferred alongshore transport under mild to moderate wave conditions at one location is consistent with sediment fluxes modelled over the entire embayment (Valiente et al., 2020). The dominance of the longshore residual transport over cross-shore transport fluxes also agrees with numerical modelling (Valiente et al., 2020) and sediment budgets (Valiente et al., 2019b) for the Perranporth embayment. Circulation patterns and resulting sediment fluxes are not spatially uniform and vary depending on wave / storm forcing because of the interaction between currents, waves, and bay geomorphology (McCarroll et al., 2018; Valiente et al., 2020). The estimated residual sediment flux appears to intensify towards the end of the study period, which also appears to be consistent with the numerical results of Valiente et al. (2020).

In absence of currents crossing the crestlines, wave-dominated ripples would mainly migrate in response to the asymmetry in the near-bed wave orbital velocities that typically occurs in shallow waters (Traykovski et al., 1999; Crawford and Hay, 2001; Soulsby and Whitehouse, 2005; Miles et al., 2014). This wave asymmetry mechanism is not included in the sediment transport equations used here. Instead, we estimated the cross-shore wave velocity skewness based on the velocity measurements in order to assess the importance of this mechanism. Results indicate close to symmetric near-bed wave velocities with values of velocity skewness being generally near zero and always below 0.35), which is consistent with the lack of wave ripple migration observed and suggest that wave-asymmetry-induced cross-shore sediment transport is not important for most of the study period (Fig. 7 d).

On the Perranporth upper shoreface, onshore ripple migration was observed because of velocity skewness (> 0.2 m/s) during mild waves with wave orbital velocities around 0.25-0.50 m/s (Miles et al., 2014). Under similar wave orbital velocities, the skewness on the lower shoreface is lower and not large enough to cause similar onshore bedform migration. Normalized velocity skewness values beyond 0.5 were correlated with ripple migration periods under non-rip current conditions at Perranporth shoreface (Thorpe et al., 2014). Even though such onshore bedform migration may be seen as a process helping beach recovery, this would not provide a pathway from the lower shoreface to the beach under mild wave conditions, but only from the upper shoreface to the beach. However, post storm recovery does not only occur during calm to mild wave conditions, high-energy wave events also appear to be essential for beach recovery after storm erosion (Scott et al., 2016). In our observations, a wave skewness around 0.2 m/s was only reached for wave orbital velocities of 0.6 m/s, when ripples were washed-out. The implication is that potential onshore wave-asymmetry-induced transport is unlikely to be related to ripple dynamics and migration, and likely to primarily occur under sheet flow conditions, thus requiring high-energy wave events. There is no evidence of wave-induced offshore sediment transport during our study period, but our deployment did not include extreme wave conditions (maximum wave height (~3 m) was well below the wave height with annual return period (~6 m)). Our observations do suggest a small offshore residual-current-related transport of sediment due to the orientation of tidal currents with respect to the shoreline, which is likely to be affected by wave-current interactions. It is, however, unclear how these separate wave and current contributions to cross-shore sediment transport balance over longer time scales (year to decade). Wave-asymmetry-generated onshore sediment fluxes under sheet flow conditions are not directly observed here and only inferred from near-bed hydrodynamics and the sediment bed state; observational confirmation of this flux would require not only new field deployments but likely new instrumentation and/or analysis techniques to accurately measure near-bed sheet flow sediment flux.

In summary, our in situ observations support the following understanding for sediment fluxes over the lower shoreface. Under calm to mild wave conditions, wave-generated onshore flux is negligible, and current supported fluxes result in significant residual alongshore and a small offshore residual. Under high energy event, wave-generated onshore flux may be possible under sheet flow conditions, and current supported fluxes are intensified both alongshore and offshore. As mentioned previously, the alongshore components are consistent with results from numerical modelling (Valiente et al., 2020) and sediment budgets (Valiente et al., 2019b). Our observations do not support the hypothesis that the lower shoreface acts as a source of sediment to the upper shoreface (and the beach) via cross-shore fluxes. Nevertheless, the cross-shore components during high energetic events could contribute to the pathways to the upper shoreface inferred by Valiente et al. (2019b).

These results provide clear evidence of small-scale seabed and sediment dynamics on the lower shoreface beyond the depth of closure, which is a typically under-sampled region (Anthony and Aagaard, 2020). For the specific embayment and lower shoreface considered, these observations support the existence of an active zone between the depth of closure and the depth of transport as proposed by Valiente et al (2019a), which would be dominated by sediment resuspended by wave stirring and subsequently transported by tidal currents. Such observations are not unexpected given that similar small-scale seabed and sediment dynamics have also been observed in deeper waters of the Celtic Sea (Thompson et al., 2017; Thompson et al., 2019).

6. Conclusions

Observed ripples on the lower shoreface of Perranporth were divided into 2D ripples (rectilinear crests) and 3D ripples (more sinusoidal or curved crests), and both 2D and 3D ripples can be considered as vortex ripples. The small-scale seabed morphology was linked to changing hydrodynamics during the study period and ripple occurrence and evolution was primarily related to wave action. Under low-energy regime, such that the threshold of motion is not reached, the seabed was static and ripples, when present, were relict ripples. For mid-energy conditions corresponding to shear stresses broadly between threshold of motion and sheet flow limit, stationary ripples were generated. The size of 2D vortex ripples increased with hydrodynamic forcing until a wash-out threshold is reached, at which point ripples abruptly transition to smaller 3D vortex ripples. The reverse transition from 3D ripples to 2D ripples is progressive with decreasing wave forcing. Under high-energy conditions, corresponding to exceedance of the sheet flow limit, ripples disappear, and sediment is inferred to be transported under sheet flow conditions.

Wave skewness was close to zero during most of the study period and no ripple migration was observed, suggesting that wave-induced cross-shore sediment transport is negligible except possibly under conditions strong enough to result in sheet flow sediment transport. Instead, sediment transport is dominated by alongshore transport by tidal currents of sediment suspended by waves over vortex ripples. This mechanism results in a northward alongshore sediment flux, as well as a small offshore component. These results do not support the hypothesis of the Perranporth lower shoreface acting as a sediment source to the upper shoreface and beach via cross-shore exchanges, and further emphasises the importance of the embayment circulation, alongshore processes, and headland bypassing (McCarroll et al., 2018; Valiente et al., 2019b; Valiente et al., 2020). However, how potential cross-shore fluxes due to wave asymmetry balance with the small offshore current-induced residual would need further investigation under high-energy conditions (sheet flow sediment transport).

7. Acknowledgements

We thank Nieves Valiente for the DEM correction and reference to Ordnance Datum Newlyn (ODN) using the Vertical Offshore Reference Frame model (VORF). We thank Richard Cooke, Emlyn Jones, and Geoff Hargreaves (NOC) and the crew of the M/V Severn Sea for the help in deploying and recovering the mini-STABLE tripod.

QG was supported by an FPI grant (ref. BES-2013-066261) from the Spanish Ministry of Economy and Competitiveness in the frame of the project FORMED (CGL2012-33989). QG was also supported by a mobility grant to develop short stays at the National Oceanography Centre, Liverpool (NOC-NERC) (ref: EEBB-I-17-11989) from the Spanish Ministry of Economy and Competitiveness. The authors wish to acknowledge funding from the Natural Environment Research Council to the BLUEcoast project (grant numbers NE/015894/1 and NE/015894/2). MEW was partially supported by Chilean Fondecyt project 11191077 and the National Research Center for Integrated Natural Disaster Management (CIGIDEN, ANID/FONDAP 15110017).

8. References

Allen, J. R. L., 1968. Current ripples: Their relation to patterns of water and sediment motion. Nord Holland, Amsterdam. 433pp

Anthony, E.J, Aagaard, T., 2020. The lower shoreface: Morphodynamics and sediment connectivity with the upper shoreface and beach, Earth-Science Reviews, 210, https://doi.org/10.1016/j.earscirev.2020.103334

Austin, M., Scott, T., Brown, J., Brown, J., MacMahan, J., Masselink, G., Russell, P., 2010. Temporal observations of rip current circulation on a macro-tidal beach. Cont. Shelf Res. 30, 1149–1165. doi:10.1016/j.csr.2010.03.005

Austin, M.J., Scott, T.M., Russell, P.E., Masselink, G., 2013. Rip Current Prediction: Development, Validation, and Evaluation of an Operational Tool. J. Coast. Res. 2, 283–300. doi:10.2112/JCOASTRES-D-12-00093.1

Baas, J.H., Best, J.L., Peakall, J., 2016. Predicting bedforms and primary current stratification in cohesive mixtures of mud and sand. J. Geol. Soc. London. 173, 12–45. doi:10.1144/jgs2015-024

Bagnold, R.A., 1946. Motion of waves in shallow water. Interaction between waves and sand bottoms. Proc. R. Soc. A Math. Phys. Eng. Sci. 187, 1–18. doi:10.1098/rspa.1946.0062

Bell, P.S., Thorne, P.D., 1997a. Measurements of sea bed ripple evolution in an estuarine environment using a high resolution acoustic sand ripple profiling system, in: Oceans '97. MTS/IEEE Conference Proceedings. pp. 339–343. doi:10.1109/OCEANS.1997.634386

Bell, P.S., Thorne, P.D., 1997b. Application of a high resolution acoustic scanning system for imaging sea bed microtopography. Seventh Int. Conf. Electron. Eng. Oceanogr. - Technol. Transf. from Res. to Ind. 128–133. doi:10.1049/cp:19970673

Bell P. S., Thorne P D., 2007. Field measurements of wave induced sand ripples in three dimensions. Published in the 'Underwater Acoustic Measurements: Technologies and results' conference CDrom, held on Crete 25-29 June at F.O.R.T.H. pp 1045-1052.

Bolaños, R., Amoudry, L.O., Doyle, K. 2011. Effects of Instrumented Bottom Tripods on Process Measurements, J. Atmos. Oceanic Tech., 28, 827-837.

Camenen, B., 2009. Estimation of the wave-related ripple characteristics and induced bed shear stress. Estuar. Coast. Shelf Sci. 84, 553–564. doi:10.1016/j.ecss.2009.07.022

Camenen, B., Larson, M., 2006. Phase-lag effects in sheet flow transport. Coast. Eng. 53, 531–542. doi:10.1016/j.coastaleng.2005.12.003.

Channel Coastal Observatory, 2020. Annual Wave Report 2017: Perranporth. Available online at: https://www.channelcoast.org/reports/index.php?link=&dla=download&id=2601&cat=128/WaveReport2017_Prp.pdf [Accessed 18 November 2020].

Clifton, H.E., Dingler, J.R., 1984. Wave-formed structures and paleoenvironmental reconstruction. Mar. Geol. 60, 165–198. doi:10.1016/S0070-4571(08)70146-8

Crawford, A.M., Hay, A.E., 2001. Linear transition ripple migration and wave orbital velocity skewness: Observations. J. Geophys. Res. 106, 14113–14128.

Dalrymple, R.W., Rhodes, R.N., 1995. Estuarine dunes and bars, in: Geomorphology and Sedimentology of Estuaries. Developments in Sedimentology. pp. 359–422.

Davidson, M.A., Turner, I.L., Splinter, K.D., Harley, M.D., 2017. Annual prediction of shoreline erosion and subsequent recovery. Coast. Eng. 130, 14–25. doi:10.1016/j.coastaleng.2017.09.008

Davies A.G., Thorne P.D., 2005. Modelling and measurement of sediment transport by waves in the vortex ripple regime. Journal of Geophysical Research. Vol 110, C05017, doi:1029/2004JC002468, 20

Davies, A. G., Thorne, P. D., 2008 Advances in the study of moving sediments and evolving seabeds, *Surveys in Geophysics*, 29 (1). 1-36.

Elgar, S., 1987. Relationships involving third movements and bispectra of a harmonic process. IEEE transctins Acoust. speech, signal Process. ASSP-35. N.

Fenton, J.D., McKee, W.D., 1990. On calculating the lengths of water waves. Coast. Eng. 14, 499–513. doi:10.1016/0378-3839(90)90032-R

Glenn, S.M., Grant, W.D., 1987. A suspended sediment stratification correction for combined wave and current flows. J. Geophys. Res. 92, 8244–8264. doi:10.1029/JC092iC08p08244

Goring, D.G., Nikora, V.I., 2002. Despiking Acoustic Doppler Velocimeter Data. J. Hydraul. Eng. 128, 117–126. doi:10.1061/(ASCE)0733-9429(2002)128:1(117)

Grant, W.D., Madsen, O.S., 1979. Combined Wave and Current Interaction With a Rough Bottom. J. Geophys. Res. 84, 1797–1808

Hamon-Kerivel, K., Cooper, A., Jackson, D, Sedrati, M, Guisado Pintado, E., 2020. Shoreface mesoscale morphodynamics: A review. Earth-Science Reviews, 209, 103330

Hanes, D.M., Alymov, V., Chang, Y.S., Jette, C., 2001. Wave-formed sand ripples at Duck, North Carolina. J. Geophys. Res. 106, 22575–22592. doi:10.1029/2000JC000337

Hurther D., Thorne P.D., 2011. Suspension and near-bed load sediment transport processes above a migrating, sand-rippled bed under shoaling waves. J. Geophys. Res., Vol 116, C07001, doi:1029/2010JC006774

Inch, K., Davidson, M., Masselink, G., Russell, P., 2017. Observations of nearshore infragravity wave dynamics under high energy swell and wind-wave conditions. Cont. Shelf Res. 138, 19–31. doi:10.1016/j.csr.2017.02.010

Kramer, K., Winter, C., 2016. Predicted ripple dimensions in relation to precision of in situ measurements in the southern North Sea. Ocean Sci. 12, 1221–1235. https://doi.org/10.5194/os-12-1221-2016.

Li, M.Z., Amos, C.L., 1998. Predicting ripple geometry and bed roughness under combined waves and currents in a continental shelf environment. Cont. Shelf Res. 18, 941–970. doi:10.1016/S0278-4343(98)00034-X

Li, M.Z., Wright, L.D., Amos, C.L., 1996. Predicting ripple roughness and sand resuspension under combined flows in a shoreface environment. Mar. Geol. 130, 139–161. doi:10.1016/0025-3227(95)00132-8

Lichtman, I. D., Baas, J. H., Amoudry, L. O., Thorne, P. D., Malarkey, J., Hope, J. A., Peakall, J., Paterson, D. M., Bass, S. J., Cooke, R. D. Manning, A. J., Davies, A. G., Parsons, D. R., Ye, L., 2018. Bedform migration in a mixed sand and cohesive clay intertidal environment and implications for bed material transport predictions. Geomorphology, 315, pp. 17–32. https://doi.org/10.1016/j.geomorph.2018.04.016

McCarroll, R.J, Masselink, G., Valiente, N.G., Scott, T., King, E.V., Conley, D. 2018. Wave and Tidal Controls on Embayment Circulation and Headland Bypassing for an Exposed, Macrotidal Site. Journal of Marine Science and Engineering, J. Mar. Sci. Eng., 6, 94; doi:10.3390/jmse6030094

Malarkey, J., Davies, A.G., 2012. A simple procedure for calculating the mean and maximum bed stress under wave and current conditions for rough turbulent flow based on Soulsby and Clarke’s (2005) method. Comput. Geosci. 43, 101–107. doi:10.1016/j.cageo.2012.02.020

Marine Electronics Ltd., 2009. User Manual for the 3D Sand Ripple Profiling Logging Sonar

Masselink, G., Scott, T., Poate, T., Russell, P., Davidson, M., Conley, D., 2016. The extreme 2013/2014 winter storms: Hydrodynamic forcing and coastal response along the southwest coast of England. Earth Surf. Process. Landforms 41, 378–391. doi:10.1002/esp.3836

Miles, J., Thorpe, A., 2015. Bedform contributions to cross-shore sediment transport on a dissipative beach. Coast. Eng. 98, 65–77. doi:10.1016/j.coastaleng.2015.01.007

Miles, J., Thorpe, A., Russell, P., Masselink, G., 2014. Observations of bedforms on a dissipative macrotidal beach. Ocean Dyn. 64, 225–239. doi:10.1007/s10236-013-0677-2

Moate, B.D., Thorne, P.D., Cooke, R.D., 2016. Field deployment and evaluation of a prototype autonomous two dimensional acoustic backscatter instrument: the Bedform And Suspended sediment Imager (BASSI). Cont. Shelf Res. 112, 78–91.

Nelson, T.R., Voulgaris, G., 2014. Temporal and spatial evolution of wave-induced ripple geometry: Regular versus irregular ripples. J. Geophys. Res. Ocean. 119, 664–688. doi:10.1002/2013JC009020.Received

Nelson, T.R., Voulgaris, G., Traykovski, P., 2013. Predicting wave-induced ripple equilibrium geometry. J. Geophys. Res. Ocean. 118, 3202–3220. doi:10.1002/jgrc.20241

Nielsen, P., 1981. Dynamics and Geometry of Wave-Generated Ripples. J. Geophys. Res. 86, 6467–6472.

Poate, T., Masselink, G., Russell, P., Austin, M., 2014. Morphodynamic variability of high-energy macrotidal beaches, Cornwall, UK. Mar. Geol. 350, 97–111. doi:10.1016/j.margeo.2014.02.004

Raudikivi, A. J. (1988). The roughness height under waves. *J. Hydr. Res.*, 26 (5), 569-584

Rousseaux, G., 2006. Physical distinction between rolling-grain ripples and vortex ripples: An experimental study. Phys. Rev. E - Stat. Nonlinear, Soft Matter Phys. 74, 1–7. doi:10.1103/PhysRevE.74.066305

Ruessink, B.G., Michallet, H., Abreu, T., Sancho, F., Werf, J.J. Van Der, Silva, P.A., 2011. Observations of velocities, sand concentrations, and fluxes under velocity - asymmetric oscillatory flows. J. Geophys. Resear 116. doi:10.1029/2010JC006443

Scott, T., Masselink, G., O'Hare, T., Saulter, A., Poate, T., Russell, P., Davidson, M., Conley, D., 2016. The extreme 2013/2014 winter storms: Beach recovery along the southwest coast of England. Mar. Geol. 382, 224–241. doi:10.1016/j.margeo.2016.10.011

Soulsby, R.L., 1983. The bottom boundary layer of shelf seas. In: Johns, B. (Ed.), Physical Oceanography of Coastal and Shelf Seas. Elsevier, Amsterdam, pp. 189–266.

Soulsby, R.L., 1997. Dynamics of marine sands. A manual for practical applications. Thomas Telford, London, ISBN 0-7277-2584-X

Soulsby, R.L., 2006. Simplified calculation of wave orbital velocities, in: Sand Transport in Oscillatory Flow. HR Wallingford, p. 12.

Soulsby, R.L., Clarke, S., 2005. Bed Shear-stresses Under Combined Waves and Currents on Smooth and Rough Beds, Estuary Processes Research Project (Est Proc)/Defra project FD1905.

Soulsby, R.L., Whitehouse, R.J.S., 2005. Prediction of Ripple Properties in Shelf Seas - Mark 1 Predictor (Report TR 150).

Soulsby, R.L., Whitehouse, R.J.S., Marten, K.V., 2012. Prediction of time-evolving sand ripples in shelf seas. Cont. Shelf Res. 38, 47–62. doi:10.1016/j.csr.2012.02.016

Styles, R., Glenn, S.M., 2005. Long-term sediment mobilization at a sandy inner shelf site, LEO-15. J.

Geophys. Res. 110. doi:10.1029/2003JC002175

Thompson, C.E.L., Silburn, B., Williams, M.E., Hull, T, Sivyer, D., Amoudry, L.O., Widdicombe, S., Ingels, J. , Carnovale, G., McNeill, C.L. , Hale, R., Laguionie Marchais, C., Hicks, N., Smith, H.E.K., Klar, J.K., Hiddink, J.G., Kowalik, J, Kitidis, V., Reynolds, S., Woodward, E.M.S., Tait, K., Homoky, W., Kröger, S., Bolam, S., Godbold, J.A., Aldridge, J., Mayor, D.J, Benoist, N.M.A., Bett, B.J., Morris, K.J., Parker E.R., Ruhl, H.A., Statham, P.J., Solan, M., 2017. An approach for the identification of exemplar sites for scaling up targeted field observations of benthic biogeochemistry in heterogeneous environments. *Biogeochemistry*, 135 (1-2), 1-34. doi: 10.1007/s10533-017-0366-1

Thompson, C..E.L.,Williams, M.E., Amoudry, L., Hull, T., Reynolds, S., Panton, A., Fones, G.R., 2019. Benthic controls of resuspension in UK shelf seas: Implications for resuspension frequency. Continental Shelf Research, 185, 3-15.

Thorne, P.D., Hanes, D.M., 2002. A review of acoustic measurement of small-scale sediment processes. Cont. Shelf Res. 22, 603–632. doi:10.1016/S0278-4343(01)00101-7.

Thorne P.D., Davies A.G., Williams J.J., 2003. Measurements of near-bed intra-wave sediment entrainment above vortex ripples. Geophysical Research Letter. Vol 30, No 20, 2028. 2.1-2.4

Thorne, P.D., Davies, A.G., Bell, P.S., 2009. Observations and analysis of sediment diffusivity profiles over sandy rippled beds under waves. J. Geophys. Res. 144

Thorne P.D. Hurther D., Cooke R.D., Barraud P.A., Barnoud J.M., Caceres I., Sanches Arcilla A., 2013. On the study of boundary layer transport processes using new developmental acoustic techniques. In: Proceeding of Coastal Dynamics 2013, held in Arachon, France, 24-28 June. pp. 1667–1676.

Thorne P.D., Hurther D., Cooke R.D, Caceres I., Barraud P.A., Sánchez-Arcilla A., 2018. Developments in acoustics for studying wave-driven boundary layer flow and sediment dynamics over rippled sand-beds. Continental Shelf Research, 166, 119-137. https://doi.org/10.1016/j.csr.2018.07.008.

Thorpe, A., Miles, J., Masselink, G., Russell, P., 2014. Bedform Dynamics in a Rip Current, Proceedings 13th International Coastal Symposium (Durban, South Africa), Journal of Coastal Research, Special Issue No. 70, pp. 700-705, ISSN 0749-0208.Thyng, K.M., C.A. Greene, R.D. Hetland, H.M. Zimmerle, and S.F. DiMarco. 2016. True colors of oceanography: Guidelines for effective and accurate colormap selection. Oceanography 29(3):9–13. http://dx.doi.org/10.5670/oceanog.2016.66

Traykovski, P., Hay, A.E., Irish, J.D., Lynch, J.F., 1999. Geometry, migration, and evolution of wave orbital ripples at LEO-15. J. Geophys. Res. 104, 1505–1524. doi:10.1029/1998JC900026

Valiente, N.G., Masselink, G., Scott, T, Conley, D., McCarroll, R.J., 2019a. Role of waves and tides on depth of closure and potential for headland bypassing, Marine Geology, 407, 60-75.

Valiente, N.G., McCarroll, R.J., Masslink, G., Scott, T., Wiggins, M., 2019b Multi-annual embayment sediment dynamics involving headland bypassing and sediment exchange across the depth of closure, Geomorphology, 343, 48-64.

Valiente, N., Masselink, G., McCarroll, R.J., Scott, T., Conley, D., King, E., 2020 Nearshore sediment pathways and potential sediment budgets in embayed settings over a multi-annual timescale. Marine Geology, 427, 106270.

van Rijn, L.C., 2007a. Unified View of Sediment Transport by Currents and Waves. I: Initiation of Motion, Bed Roughness, and Bed-Load Transport. J. Hydraul. Eng. 133, 649–667. doi:10.1061/(ASCE)0733-9429(2007)133:7(776)

van Rijn, L.C., 2007b. Unified View of Sediment Transport by Currents and Waves. II: Suspended

Tranport. J. Hydraul. Eng. 133, 668–689. doi:10.1061/(ASCE)0733-9429(2007)133:7(776)

Wiberg, P.L., Nelson, J.M., 1992. Unidirectional flow over asymmetric and symmetric ripples. J. Geophys. Res. 97, 12745–12761. doi:10.1029/92JC01228

Wiberg, P.L., Sherwood, C.R., 2008. Calculating wave-generated bottom orbital velocities from surface-wave parameters. Computers and Geosciences, 34, 1243-1262

Wright, L.D., Short, A.D. 1984. Morphodynamic variability of surf zones and beaches: A synthesis, Marine Geology, 56, 1–4, 93-118, https://doi.org/10.1016/0025-3227(84)90008-2.

Wright, L.D., Boon, J.D., List, J.H., 1991. Models of cross-shore sediment transport on the shoreface of the Middle Atlantic Bight. Mar. Geol. 96, 19–51. doi:10.1016/0025-3227(91)90200-N

Xiong, J., Wang, Y.P., Gao, S., Du, J., Yang, Y., Tang, J., Gao, J. 2018. On estimation of coastal wave parameters and wave-induced shear stresses. Limnol Oceanogr. Methods, 16 (9), 594-606